AVEY BIDIRECTIONAL ARCHITECTURE

Anonymous authors
Paper under double-blind review

ABSTRACT

Compact pretrained bidirectional encoders remain the backbone of industrial NLP under tight compute and memory budgets. Their effectiveness stems from self-attention's ability to deliver bidirectional contextualization with high parallelism, as popularized by BERT-style architectures. Recently, *Avey* was introduced as an autoregressive, attention-free alternative that naturally admits an encoder-only adaptation. In this paper, we reformulate Avey for the encoder-only paradigm and propose several innovations to its architecture, including decoupled static and dynamic parameterizations, stability-oriented normalization, and neural compression. Results show that this reformulated architecture compares favorably to four widely used Transformer-based encoders, consistently outperforming them on standard token-classification and information-retrieval benchmarks while scaling more efficiently to long contexts.

1 INTRODUCTION

Pretrained bidirectional Transformer encoders, most notably BERT (Devlin et al., 2019), have been especially impactful in resource-constrained, application-specific settings, where compact models can be efficiently fine-tuned for downstream tasks and deployed under strict latency and memory budgets. Unlike unidirectional Transformer decoders, bidirectional encoders condition each token on both its left and right contexts, yielding fully contextualized representations that improve disambiguation and translate into stronger performance on certain discriminative tasks (e.g., classification, retrieval, and extractive question-answering) (Liu et al., 2019; Wang et al., 2019b;a; Karpukhin et al., 2020; Khattab & Zaharia, 2020; Rajpurkar et al., 2016; 2018). Since BERT's introduction, such encoders have seen broad and sustained adoption across academia and industry (Muennighoff et al., 2023; Thakur et al., 2021; Santhanam et al., 2022; Wang et al., 2022; Su et al., 2023), particularly targeting high-throughput, high-precision, and budget-constrained applications (Lan et al., 2020; Sanh et al., 2019; Sun et al., 2020; Jiao et al., 2020).

The BERT family's success in research and industry was enabled by the Transformer (Vaswani et al., 2017), whose self-attention mechanism affords bidirectional contextualization while maintaining high parallelizability. However, the quadratic time and memory costs of full self-attention remain a central bottleneck (Tay et al., 2022; Munkhdalai et al., 2024), limiting practical extension of context windows in cost-sensitive deployments. A large body of work has sought to mitigate this bottleneck (e.g., via using linear attention (Katharopoulos et al., 2020; Choromanski et al., 2021; Peng et al., 2025) and RNN-inspired architectures (Gu et al., 2021; Gupta et al., 2022; Fu et al., 2022; Gu & Dao, 2023)), but little of it has been adapted to the bidirectional, encoder-only paradigm. Meanwhile, BERT itself was modernized through larger pretraining corpora, architectural refinements (e.g., FlashAttention (Dao et al., 2022), SwiGLU activations (Shazeer, 2020), and RoPE positional encoding (Su et al., 2021)), and new pretraining and fine-tuning strategies (Liu et al., 2019; Portes et al., 2023; Warner et al., 2025), among others.

Most recently, Avey (Hammoud & Acharya, 2025) was introduced as an autoregressive architecture that departs from both Transformer- and RNN-based designs. It partitions a sequence into splits, ranks and retrieves the most relevant splits for each target split, and applies a dynamically parameterized neural processor to contextualize them. By decoupling context width from sequence length, Avey enables efficient long-range interactions and extrapolation far beyond its training window, facilitating practical context extensions at realistic compute budgets.

To elaborate on its technical aspects, Avey is a recurrence- and attention-free architecture comprising two principal components, a ranker and a neural processor. The ranker slices each input sequence into splits of consecutive tokens and selects the top k most relevant splits for each current split being processed by the neural processor. The neural processor consists of three core units, the enricher, contextualizer, and fuser. The enricher enhances the quality of token embeddings by expanding their learnable features using a position-wise neural network. The contextualizer is an embedding-wise neural network with dynamic parameterization and cosine-similarity–based selectivity, enabling interactions between relevant tokens across the current and top k splits. Lastly, the fuser learns a function that integrates the contextualized features produced by the contextualizer with some uncontextualized features bypassed by a partial-embedding bypassing mechanism.

Although originally formulated for causal language modeling, Avey's cosine-similarity–based selectivity and learned cross-embedding linear transformation make it naturally amenable to a bidirectional, encoder-style adaptation. In this paper, we introduce **Avey–B**, a bidirectional reformulation of Avey for the encoder-only setting, and compare it empirically against widely used and recently introduced Transformer-based encoders, namely, BERT (Devlin et al., 2019), RoBERTa (Liu et al., 2019), ModernBERT (Warner et al., 2025), and NeoBERT (Breton et al., 2025). We further propose architectural advances that enhance its effectiveness and efficiency, including: (1) decoupled static and dynamic parameterizations; (2) a stability-oriented, row-normalized similarity scores in the dynamic layers; and (3) a compression module that reduces retrieved context before contextualization in the neural processor.

Concretely, Avey-B contextualizes tokens via either a learned static linear projection *or* a dynamic similarity matrix computed from cosine similarities, *in any given layer*. This contrasts with Avey, which multiplicatively couples the learned projection with cosine scores element-wise *in every layer*. By decoupling the static and dynamic parameterizations, Avey-B avoids destructive interactions between fixed weights and input-dependent scores, most notably inversion effects where a token highly similar to a neuron's current token is forced to contribute less than a less-similar one. In addition, we normalize the cosine scores at each position by the sum of that position's scores over all tokens, stabilizing training and consistently improving downstream task performance.

Alongside, we observe that extending Avey to the bidirectional paradigm without some modifications may introduce a scalability issue. Specifically, in the original design of Avey, each split is concatenated with its top-k relevant splits and jointly contextualized in a single pass through the neural processor. Performing this for *every* split inflates the input size to roughly k times the number of tokens, substantially increasing processing time. In the autoregressive regime, this overhead is mitigated by training on short context widths, leveraging Avey's ability to extrapolate well beyond that. It is also tolerable at inference because *only* the most recent split is contextualized with its top-k splits to generate the next token. In the bidirectional inference setting, however, this strategy is infeasible, since *all* splits must be contextualized to produce complete token-level representations.

Building on this observation and recognizing that inference efficiency is critical for encoder models (especially in industry where they are commonly used (Raghavan, 2020; Zhu, 2019; Guo et al., 2020; Warner et al., 2025)), we introduce a neural compression scheme in the ranker. More precisely, we compress each split together with its top-k retrieved splits back to the size of a single split via a learned linear projection. As a result, the neural processor contextualizes only as many tokens as in the original input sequence, avoiding redundant computations over the appended top-k splits. Because the neural processor operates on each split independently, Avey-B achieves higher throughput than Transformer-based encoders, while preserving high accuracy across a wide range of downstream benchmarks.

To summarize, our main contributions in this paper are as follows:

- We propose Avey-B, a bidirectional encoder architecture that capitalizes on Avey by decoupling static and dynamic parameterizations and introducing a lightweight normalization scheme for dynamic contextualization.

- We redesign Avey's ranker to compress each split's top-k retrieved context into a fixed token budget, making the neural processor's per-split compute independent of k while preserving the benefits of retrieving larger relevant token sets via increasing k.

- We conduct extensive design-choice and ablation studies to identify the most effective architectural configuration and demonstrate how each proposed idea contributes to the performance gains of Avey-B over the original Avey architecture.
- We show that Avey-B outperforms BERT (Devlin et al., 2019) and NeoBERT (Breton et al., 2025) across all the evaluated benchmarks, and consistently surpasses RoBERTa (Liu et al., 2019) and ModernBERT (Warner et al., 2025) on token-classification and information-retrieval tasks, despite being pretrained on $\sim 11\times$ fewer tokens than ModernBERT.
- We illustrate that Avey-B scales efficiently with sequence length, yielding substantially lower latency than Transformer-based encoders. Across 128–96 K tokens, Avey-B is consistently faster than all the evaluated Transformer baselines, and its advantage *widens* with sequence length N. For example, at $N = 96\,\text{K}$, Avey-B outpaces ModernBERT and NeoBERT by $3.38\times$ and $11.63\times$, respectively.
- A power-law fit, $T(N) \propto N^{-\alpha}$, yields a markedly smaller decay exponent for Avey-B ($\alpha \approx 0.44$) compared to ModernBERT ($\alpha \approx 0.77$) and NeoBERT ($\alpha \approx 0.81$), indicating that Avey-B's throughput decreases at only about half the rate of ModernBERT (and even more slowly relative to NeoBERT) as sequence length increases.
- We release the full implementation and pretrained checkpoints of Avey-B (see Section 7), enabling reproducibility and fostering future research.

The rest of the paper is organized as follows. Section 2 reviews related work, and Section 3 provides background on Avey. We elaborate on the Avey-B architecture, including its bidirectional contextualization, decoupled parameterization, and neural compression in Section 4. Section 5 presents our experimental setup, design choices and ablations, and effectiveness and efficiency results. Finally, we conclude in Section 6.

2 Related Work

The introduction of GPT (Radford et al., 2018) in 2018 marked a turning point in large-scale language modeling, establishing the now-standard paradigm of pretraining Transformer-based models on massive unlabeled corpora followed by supervised fine-tuning on task-specific data. GPT optimized a causal language modeling (CLM) objective, pretraining a unidirectional, decoder-only Transformer (Vaswani et al., 2017) for next-token prediction. The resulting pretrained model can then be effectively fine-tuned with modest labeled data to a broad range of downstream tasks, including text classification (Wang et al., 2019b), natural language inference (Bowman et al., 2015; Williams et al., 2018), and question answering (Rajpurkar et al., 2016; Lai et al., 2017), to mention just a few. This pretrain–fine-tune paradigm yielded state-of-the-art performance on these tasks at the time (Radford et al., 2018).

BERT (Devlin et al., 2019) extended this paradigm by replacing the unidirectional decoder with a fully bidirectional encoder. Concretely, it introduced two pretraining objectives, masked language modeling (MLM), which reconstructs randomly masked tokens in an input sequence, and next sentence prediction (NSP), which models inter-sentence relationships. By contextualizing tokens in both directions, BERT delivered substantial gains over causally pretrained models, particularly on benchmarks such as GLUE (Wang et al., 2019b), MultiNLI (Williams et al., 2018), and SQuAD (Rajpurkar et al., 2016), among others.

RoBERTa (Liu et al., 2019) robustly optimized BERT by retaining its overall architecture while systematically revisiting nearly every aspect of its pretraining setup. Key modifications included removing the NSP objective, pretraining with larger batches and longer sequences, adopting dynamic masking strategies, and scaling to substantially larger corpora. Building on this foundation, DeBERTa (He et al., 2021b;a; 2023) introduced disentangled attention, which separates content and positional information into distinct attention matrices, and improved fine-tuning stability through virtual adversarial training. Together, these innovations further advanced performance on some challenging benchmarks such as SuperGLUE (Wang et al., 2019a).

Subsequent work emphasized both architectural refinements and pretraining efficiency. For example, MosaicBERT (Portes et al., 2023) integrated FlashAttention (Dao et al., 2022), ALiBi positional biases (Press et al., 2022), and gated linear units (GLU) (Dauphin et al., 2017; Shazeer, 2020) to accelerate pretraining while maintaining strong downstream accuracy. NomicBERT (Nussbaum et al.,

2024) adopted SwiGLU (Shazeer, 2020) and rotary positional encodings (RoPE) (Su et al., 2021). NeoBERT (Breton et al., 2025) combined RoPE, SwiGLU, and RMSNorm (Zhang & Sennrich, 2019) with depth–width rebalancing and large-scale pretraining. ModernBERT (Warner et al., 2025) pushed this trend further, employing many of these techniques (e.g., RoPE, FlashAttention, and alternating global/local attention), supporting context windows for up to 8,192 tokens, and pretraining on multi-trillion-token corpora.

All of the above models are Transformer-based, leveraging self-attention to provide effective bidirectional contextualization while maintaining high pretraining parallelism. Recently, a fundamentally different architecture named Avey (Hammoud & Acharya, 2025) was introduced. Avey is attention-free and can process virtually unlimited sequence lengths (see Section 3). Avey-B capitalizes on Avey to support bidirectional contextualization, mirroring the shift from GPT-style decoder-only to BERT-style encoder-only models in the Transformer family. We empirically compare Avey-B against BERT, RoBERTa, ModernBERT, and NeoBERT in Section 5.

3 Background

The original Avey architecture decouples sequence length from context width by pairing a lightweight ranker with a data-dependent neural processor. We next provide a background on both.

3.1 Ranker

Avey partitions an input sequence of length N into equal-sized *splits* of S tokens, applying zero-padding if N is not divisible by S. For a given *current* split, the ranker computes its relevance to each preceding split using the MaxSim operator (Khattab & Zaharia, 2020), orders them by their MaxSim scores, and selects the top-k splits for contextualization.

Before contextualization, the MaxSim scores of the top-k selected splits are normalized by dividing each score by the maximum among them. Each selected split is then weighted by its normalized score and concatenated with the current split. This *weighted-selective-split* mechanism prunes irrelevant global tokens and scales the contribution of each retrieved split based on relevance.

Crucially, the ranker is invoked only *once* per full forward/backward pass, independent of the number of neural-processor layers. Matching each split against all preceding splits yields a training-time compute cost of $\mathcal{O}(N^2 d)$, where d is the embedding dimension.

3.2 Neural Processor

The neural processor ingests the current split and its weighted top-k retrieved splits, and processes them through a layered architecture. Each layer comprises three modules, an **enricher**, a **contextualizer**, and a **fuser**.

The enricher is a single-layer, position-wise neural network applied independently to each token embedding. Given C input embeddings arranged as $\mathbf{X} \in \mathbb{R}^{C \times d}$, the enricher computes a matrix $\mathbf{Z} \in \mathbb{R}^{C \times m}$ (with $m > d$) as follows:

$$\mathbf{Z} \;=\; \sigma\big(\mathbf{X}\mathbf{U} + \mathbf{b}\big), \tag{1}$$

where $\mathbf{U} \in \mathbb{R}^{d \times m}$ is a learnable weight matrix, $\mathbf{b} \in \mathbb{R}^{C \times m}$ represents biases, and $\sigma(\cdot)$ is an activation function. The output $\mathbf{Z}$ is partitioned into a *head* $\mathbf{Z}_h \in \mathbb{R}^{C \times m_h}$, which is bypassed directly to the fuser, and a *tail* $\mathbf{Z}_t \in \mathbb{R}^{C \times m_t}$ (with $m = m_h + m_t$), which is forwarded to the contextualizer. This *partial-embedding bypassing* technique preserves raw token-specific features and mitigates degradation effects (e.g., over-smoothing), as the number of layers is increased.

The contextualizer operates on the tail $\mathbf{Z}_t$. Each m_t-dimensional tail embedding is split evenly into a *gating* left half and a *contextual* right half, yielding $\mathbf{Z}_{tl} \in \mathbb{R}^{C \times \frac{m_t}{2}}$ and $\mathbf{Z}_{tr} \in \mathbb{R}^{C \times \frac{m_t}{2}}$, respectively. Formally, the contextualizer is a single-layer, embedding-wise network that updates $\mathbf{Z}_{tr}$ as follows:

$$\mathbf{c}(\mathbf{Z}_t) \;=\; \mathbf{Z}_{tl} \;\odot\; \sigma\Big(\big(\mathbf{V} \;\odot\; \mathcal{N}(\mathbf{Z}_{tr})\mathcal{N}(\mathbf{Z}_{tr})^\top\big)\,\mathbf{Z}_{tr} \;+\; \mathbf{b}'\Big), \tag{2}$$

where $\mathbf{V} \in \mathbb{R}^{C \times C}$ is a learned cross-embedding matrix, $\odot$ denotes element-wise (Hadamard) multiplication, $\mathcal{N}(\cdot)$ applies row-wise ℓ_2 normalization (so $\mathcal{N}(\mathbf{Z}_{tr})\mathcal{N}(\mathbf{Z}_{tr})^\top$ computes cosine similarities between embeddings), and $\mathbf{b}'$ is an optional bias. Intuitively, each neuron aggregates statically

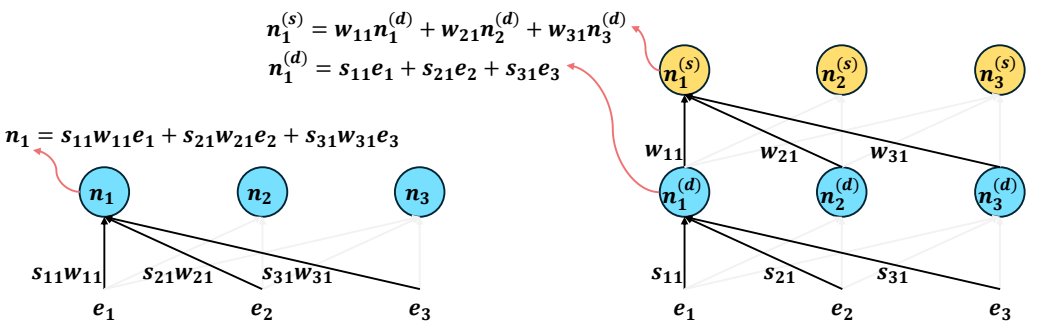

(a) Avey's *Coupled* Parametrization **(b) Avey-B's *Decoupled* Parametrization**

Figure 1: A simple illustration of coupled (a) and decoupled (b) parameterizations (e_i = embedding i; s_{ij} = cosine similarity score between e_i and e_j; n_i = neuron i, ${n_i}^{(d)}$ = neuron i in dynamic layer d; ${n_i}^{(s)}$ = neuron i in static layer s; and w_{ij} = weight corresponding to e_i or ${n_i}^{(d)}$ used in the weighted sum of n_j or ${n_j}^{(s)}$, respectively).

and dynamically weighted contributions from other embeddings, and the resulting update is gated by $\mathbf{Z}_{tl}$. The learned matrix $\mathbf{V}$ provides position-sensitive mixing, so no additional positional encodings are required within the contextualizer.

The fuser combines the bypassed and contextualized streams and projects the output back to the model embedding dimension d as follows:

$$f(\mathbf{Z}) \;=\; [\,\mathbf{Z}_h \,\|\, \mathbf{c}(\mathbf{Z}_t)\,]\,\mathbf{O}, \tag{3}$$

where $\mathbf{O} \in \mathbb{R}^{(m_h+m_t/2)\times d}$ is a learned projection matrix. As with the enricher, the fuser is applied independently to each token embedding. Its output is merged with the enricher's input within the same layer via a residual, element-wise addition.

Aggregating the costs of the ranker, enricher, contextualizer, and fuser over L layers yields a training complexity of $\mathcal{O}(N^2 d)$ for an input sequence of length N. At inference, only the most recent split is contextualized for autoregressive decoding, reducing the complexity to $\mathcal{O}(N)$.

4 Avey-B

Avey-B is a bidirectional reformulation of Avey. We next elaborate on its architecture and computational implications.

4.1 Bidirectional Contextualization

Avey-B drops the autoregressive mask in Avey's contextualizer, allowing each token representation to condition on both left and right contexts. Specifically, when a split is contextualized with its top-k selected splits, all token interactions are permitted, without any causal masking. This converts Avey into an encoder-style architecture while preserving selective global access via the ranker.

4.2 Decoupled Parametrization

In Avey, the contextualizer multiplies (element-wise) a learned, static weight matrix (i.e., $\mathbf{V}$) with an input-dependent cosine-similarity matrix (i.e., the outcome of $\mathcal{N}(\mathbf{Z}_{tr})\mathcal{N}(\mathbf{Z}_{tr})^\top$), then uses the result to linearly combine the input embeddings (i.e., $\mathbf{Z}_{tr}$) into contextualized representations (see Equation 2). This tight coupling of fixed parameters with data-driven relevance scores can induce pathological behaviors. For instance, a token that is highly similar to a neuron's current token (thus, yielding a positive cosine score) can be forced to contribute negatively whenever the corresponding entry of $\mathbf{V}$ is negative. Consequently, the neuron's update violates *monotonicity with respect to relevance*, which entails that a more-relevant token must contribute at least as much as a less-relevant one, and increasing a token's relevance must not reduce or invert its contribution.

Fig. 1 (a) offers a simple illustration of the problem. Suppose the cosine similarity s_{21} exceeds s_{31}; then embedding e_2 should contribute at least as much to neuron n_1's update as embedding e_3.

In Avey's coupled design, the element-wise product with learned weights can invert this ordering. Specifically, if weight $w_{31} \gg$ weight w_{21} (or the signs differ), the effective contributions $w_{21}s_{21}$ and $w_{31}s_{31}$ can be reversed (especially at inference), undermining evidence accumulation from the most informative tokens.

Avey-B addresses this problem by *decoupling* the two parameter sources (i.e., learned weights and input-driven similarities) and interleaving them across depth (we compare different interleaving patterns in Appendix D). In particular, we define each layer to be either *static* or *dynamic*. A static layer applies a learned linear transformation on embeddings while a dynamic layer weights them solely by cosine similarity. Alternating these layers preserves monotonicity of similarity-based updates with respect to relevance (i.e., when $s_{21} > s_{31}$, token 2 receives no smaller, and typically larger, positive influence than token 3 in the dynamic layer).

Fig. 1 (b) demonstrates the effect of decoupled parametrization. If $s_{21} > s_{31}$, the dynamic layer for neuron $n_1^{(d)}$ assigns a larger normalized weight to e_2 than to e_3, with no learned weights intervening in this similarity-based update. In the following static layer (assuming an interleaved dynamic-static pattern) for $n_1^{(s)}$, both contributions are scaled by the same coefficient w_{11}; hence, the ordering established by the dynamic layer is preserved. More generally, because the static layer is similarity-agnostic, it cannot retroactively modify the normalized dynamic scores or introduce similarity-conditioned sign flips.

To this end, decoupling static and dynamic computations maintains the *monotonicity guarantee* at each dynamic layer while still allowing representation shaping in static layers. Static layers will, of course, change the representations from which subsequent similarities are computed, but they do not alter the scores already assigned by a preceding dynamic layer and thus do not violate monotonicity for that layer. We provide a formal proof for this monotonicity guarantee in Appendix A and ablate this decoupling design choice in Appendix H. We further analyze the coupled versus decoupled parameterizations and their implications in Appendix L.

Formally, let $\mathbf{Z}_{\mathrm{tr}} \in \mathbb{R}^{C \times d'}$ denote the matrix of contextual, right-tail components for C enriched embeddings, where d' is the contextualizer's right-tail dimension (see Section 3 for more information on all notations). In Avey-B, a static layer applies a learned cross-embedding linear transformation as follows:

$$\mathbf{c}_{\mathrm{static}}(\mathbf{Z}) \;=\; \sigma\big(\mathbf{V}\,\mathbf{Z}_{\mathrm{tr}} + \mathbf{b}^{(s)}\big), \tag{4}$$

where $\mathbf{V} \in \mathbb{R}^{C \times C}$ is a learned matrix, $\mathbf{b}^{(s)} \in \mathbb{R}^{C \times d'}$ is an optional bias, and $\sigma(\cdot)$ is an activation function. Intuitively, each neuron first aggregates linearly the C embeddings and then applies the pointwise activation σ.

On the flip side, an Avey-B's dynamic layer computes an input-dependent similarity matrix from $\mathbf{Z}_{\mathrm{tr}}$ and utilizes it to mix embeddings as follows:

$$\mathbf{S} \;=\; \mathcal{N}(\mathbf{Z}_{\mathrm{tr}})\,\mathcal{N}(\mathbf{Z}_{\mathrm{tr}})^{\top} \;\in \mathbb{R}^{C \times C}, \tag{5}$$

$$\widetilde{\mathbf{S}}_{i,j} \;=\; \frac{\mathbf{S}_{i,j}}{\sum_{j=1}^{C} \mathbf{S}_{i,j} + \varepsilon} \qquad \text{(row-wise sum normalization)}, \tag{6}$$

$$\mathbf{c}_{\mathrm{dyn}}(\mathbf{Z}) \;=\; \sigma\big(\,\widetilde{\mathbf{S}}\,\mathbf{Z}_{\mathrm{tr}} + \mathbf{b}^{(d)}\,\big). \tag{7}$$

Here $\mathcal{N}(\cdot)$ denotes per-row ℓ_2 normalization to unit length so that $\mathbf{S}$ encodes cosine similarities; $\varepsilon > 0$ is a small stabilizer ensuring a positive denominator; $\mathbf{b}^{(d)} \in \mathbb{R}^{C \times d'}$ is an optional bias, and $\widetilde{\mathbf{S}}$ is a simple *sum-normalized* similarity matrix. This row-wise normalization yields a row-stochastic similarity operator (row sums ≤ 1), which bounds per-row gain and mitigates the growth of large singular values through depth, improving numerical conditioning and trainability. In the unnormalized case (i.e., in Avey), inflated singular values can drive activation and gradient growth with depth, resulting in unstable optimization and degraded generalization. We ablate this normalization technique and show consistent gains over softmax-based and RMS-style alternatives in Appendix E.

4.3 NEURAL COMPRESSION

A key bottleneck in extending Avey to the bidirectional setting is the per-split concatenation strategy, whereby each current split is concatenated with its top-k retrieved splits for contextualization. This is manageable in Avey's autoregressive inference because only the most recent split is expanded. In the bidirectional regime, however, every split within the contextualizer's window must be expanded, which inflates the effective sequence length by a factor of $k + 1$.

To mitigate this, Avey-B introduces a neural compressor within the ranker to condense the concatenated $(k + 1)S$-token block back to S tokens, where S denotes the split size. Specifically, the compressor is an embedding-wise neural module that maps the $(k+1)S$ input tokens to S representative tokens, effectively distilling cross-split information before it is passed to the neural processor. To preserve signal from the block's current split, Avey-B adds a residual connection between the compressor output and the split's original S tokens, which improves stability and downstream effectiveness. An ablation studying the impact of this residual on Avey-B's accuracy is presented in Appendix H.

Formally, let $\mathbf{X}_{\text{cat}} \in \mathbb{R}^{(k+1)S \times d}$ be the concatenation of a *single* split with its top-k retrieved splits, where d denotes the embedding dimension. Subsequently, Avey-B produces a compressed output $\widehat{\mathbf{X}} \in \mathbb{R}^{S \times d}$ as follows:

$$\widehat{\mathbf{X}} \;=\; \mathbf{P}\,\mathbf{X}_{\text{cat}} \tag{8}$$

where $\mathbf{P} \in \mathbb{R}^{S \times (k+1)S}$ is a learnable matrix that performs a linear cross-token transformation, and $\widehat{\mathbf{X}}$ replaces $\mathbf{X}_{\text{cat}}$ as the input to the neural processor. Because $\mathbf{P}$ is a learned matrix, the compressor can preserve globally informative content while discarding potential redundancy, yielding a favorable accuracy/throughput trade-off. We study the effect of the compressor on Avey-B's accuracy and throughput in Appendix H.

As discussed in (Hammoud & Acharya, 2025), computation in the neural processor largely dominates that of the ranker. As such, when Avey-B reduces the number of tokens contextualized per split from $(k+1)S$ to S, throughput improves by $4.37\times$ (see Fig. 3 in Appendix H), albeit leaving Avey's asymptotic complexity unchanged (still quadratic with respect to the sequence length N).

5 EXPERIMENTS

5.1 EXPERIMENTAL SETUP

In this section, we compare Avey-B with widely used and recently introduced Transformer-based encoders, namely, BERT (Devlin et al., 2019), RoBERTa (Liu et al., 2019), ModernBERT (Warner et al., 2025), and NeoBERT (Breton et al., 2025). We evaluate two Avey-B model sizes, *base* and *large*, each pretrained on 180B tokens drawn from the FineWeb corpus (Hugging Face, 2023). Pretraining details and information about all the evaluated models are provided in Appendix B.

To assess effectiveness, we adopt the evaluation protocol of Boukhlef *et al.* (Gisserot-Boukhlef et al., 2025), targeting breadth across four downstream categories prevalent in practice, including Sequence Classification (SC), Token Classification (TC), Question Answering (QA), and Information Retrieval (IR). Each category is represented by three established benchmarks, namely, MNLI (Williams et al., 2018), QQP (Wang et al., 2017), and SST-2 (Socher et al., 2013) under SC; CoNLL-2003 (Sang & De Meulder, 2003), OntoNotes (Hovy et al., 2006), and UNER (Mayhew et al., 2023) under TC; ReCoRD (Wang et al., 2019a), SQuAD (Rajpurkar et al., 2016), and SQuAD-v2 (Rajpurkar et al., 2018) under QA; and MLDR (Multi-Granularity, 2024), MS MARCO (Bajaj et al., 2016), and NQ (Kwiatkowski et al., 2019) under IR.

We fine-tuned benchmarks under SC and TC for 1 epoch, QA for 4 epochs, and IR for 1,000 optimization steps. For each benchmark, we swept four learning rates $\{2 \times 10^{-5}, 6 \times 10^{-5}, 1 \times 10^{-4}, 5 \times 10^{-4}\}$ and trained each configuration with 10 independent random seeds. Akin to (Liu et al., 2019), the reported results for each model are the *median* scores across seeds at the *best* learning rate. SC is evaluated with accuracy, TC and QA with F1 score, and IR with NDCG@10. Lastly, following Boukhlef *et al.* (Gisserot-Boukhlef et al., 2025), we used linear learning-rate decay with warmup over the first 10% of steps.

Table 1: Design and masked language modeling (MLM) choices.

Question	Answer	Experiments
What is the most effective arrangement of static (S) and dynamic (D) layers?	Interleaved layers with a repeating $S \rightarrow D$ pattern	Appendix D
What is the most effective normalization technique within the dynamic layers, Softmax, RMS Norm, or Row-wise normalization?	Row-wise normalization	Appendix E
What are the best values for sequence length N, split size S, and top k splits?	$N = 2048$, $S = 256$, $k = 3$	Appendix F
Should the ranker operate bidirectionally as well?	No	Appendix C
What is the best masking rate?	20%	Appendix G

Table 2: Effectiveness results for several encoders at different scales (M = Medium).

	Model	SC				TC				QA				IR			
		MNLI	QQP	SST-2	**Avg.**	CONLL	Onto.	UNER	**Avg.**	ReCoRD	SQuAD	SQuAD v2	**Avg.**	MLDR	MS MARCO	NQ	**Avg.**
Base	Avey-B	83.58	**89.81**	**92.94**	88.78	**92.88**	**93.80**	**94.10**	**93.59**	44.03	74.44	68.88	62.45	**63.83**	**88.14**	**83.62**	**78.53**
	BERT	81.92	88.57	90.94	87.14	90.25	91.03	88.20	89.82	36.76	72.20	63.99	57.65	57.42	81.15	80.66	73.08
	RoBERTa	86.42	89.12	92.78	89.44	90.55	92.11	88.16	90.27	**67.86**	**80.68**	76.62	**75.05**	56.07	86.47	80.30	74.28
	ModernBERT	**86.72**	89.81	92.32	**89.61**	92.30	93.74	92.30	92.78	65.73	80.23	**77.36**	74.44	54.29	88.09	75.24	72.54
M	NeoBERT	82.53	88.88	84.69	85.36	87.55	88.88	88.17	88.20	37.74	64.84	64.42	55.67	39.98	70.76	59.43	56.72
Large	Avey-B	85.66	89.22	94.38	89.75	**93.60**	**94.09**	**94.32**	**94.00**	58.22	77.30	72.46	69.32	**67.05**	88.72	**86.24**	**80.67**
	BERT	85.08	89.27	92.26	88.87	88.54	90.71	86.09	88.44	52.02	77.93	72.96	67.64	61.08	87.71	85.42	78.07
	RoBERTa	90.16	89.49	94.67	91.44	91.71	92.70	88.79	91.07	**80.86**	**84.00**	**83.04**	**82.63**	58.50	**89.43**	85.91	77.95
	ModernBERT	**90.53**	**90.73**	**95.99**	**92.41**	92.43	93.79	92.92	93.05	73.05	82.02	79.96	78.34	59.64	88.82	81.36	76.61

To measure efficiency, we report *latency* (seconds/forward pass) and *throughput* (tokens/second) as a function of input context length (with a fixed batch size of 8), benchmarking models on NVIDIA H200 GPUs under identical software and precision settings. These measurements provide a direct comparison of scalability and deployment efficiency between Avey-B and Transformer-based encoders.

5.2 Design Choices and Ablations

Following the methodology established in the original Avey work (Hammoud & Acharya, 2025), we conduct systematic design–choice studies to identify effective configurations for Avey-B. We also sweep the masking rate to select a robust setting for pretraining Avey-B. Table 1 summarizes these studies and links to the supporting experiments for each conclusion.

Moreover, we perform ablation studies to quantify the contribution of each refinement to Avey-B. Specifically, we measure incremental gains from: (1) decoupling and interleaving static and dynamic parameterizations, (2) introducing normalization within the dynamic layers, and (3) integrating a neural compressor into the ranker. Appendix H presents the full results and analysis.

5.3 Effectiveness

We now evaluate Avey-B on standard SC, TC, QA, and IR benchmarks, comparing it against BERT, RoBERTa, ModernBERT, and NeoBERT. For all baselines we consider *base* and *large* configurations (see Table 3 in Appendix B), except for NeoBERT which is evaluated on its only publicly available size, that is, *medium*. Table 2 summarizes all the results.

At the *base* scale (and *medium* for NeoBERT), Avey-B surpasses BERT and NeoBERT across all task categories, despite using ∼85M fewer parameters than NeoBERT. It also delivers the strongest results on TC and IR, outperforming *all* Transformer-based models in both categories. For SC, Avey-B attains the best scores on QQP (tied with ModernBERT) and SST-2, while trailing RoBERTa and ModernBERT on MNLI. For QA, Avey-B leads on SQuAD-v2 but lags RoBERTa and ModernBERT on ReCoRD and SQuAD.

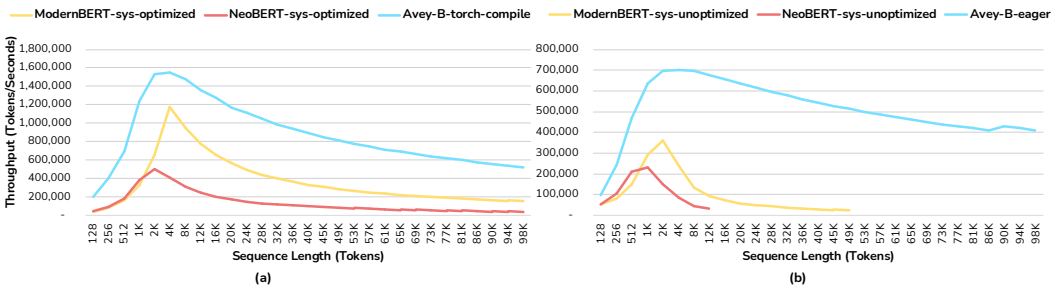

Figure 2: Throughput of Avey-B, ModernBERT, and NeoBERT on NVIDIA B200 GPUs with mixed precision (BF16). We use Avey-B *base*, ModernBERT *base*, and NeoBERT *medium* (the only publicly available size). Avey-B is shown in (a) as optimized using `torch.compile` (no fused-kernel implementation is available yet) and in (b) as unoptimized (eager). For ModernBERT and NeoBERT, throughput is shown for system–optimized (*with* FlashAttention) and system–unoptimized (eager) variants in (a) and (b), respectively.

At the *large* scale (and *medium* for NeoBERT), Avey-B again outperforms BERT and NeoBERT across all task categories. It also offers the strongest results on TC and IR, surpassing *every* Transformer-based model. Notably, the Avey-B *base* model even exceeds all *large* Transformer encoders on TC and IR (despite also being pretrained on $\sim 11\times$ fewer tokens than ModernBERT, for example). These results highlight Avey-B's advantage for both local, span-sensitive decisions (TC) and long-document encoding (IR).

In summary, at both *base* and *large* scales, Avey-B exceeds BERT and NeoBERT on every evaluated benchmark and delivers consistent gains over all baselines on TC and IR. We attribute these gains to two design factors: (1) TC tasks hinge on local evidence within short spans, and Avey-B's split-based processing with pruning of low-relevance splits/tokens sharpens the signal-to-noise ratio; and (2) IR benefits from selectively pairing globally relevant content with its immediate local context when encoding long documents (an inductive bias Avey-B enforces by construction), whereas full bidirectional processing over all tokens (like in all the Transformer-based models) tends to admit distractors and dilute relevance as sequence length grows.

5.4 Efficiency

Avey is a recent architecture and still lacks a fused-kernel (CUDA/Triton) implementation. Consequently, we evaluate its inference efficiency using `torch.compile`, which performs graph capture and backend code generation but stops short of handcrafted, specialized fused kernels available to mature Transformer encoders. We denote this configuration as *Avey-B-torch-compile*. To quantify compilation gains and offer a reference without compiler optimizations, we also report Avey-B's efficiency in the *eager* PyTorch mode, referred to as *Avey-B-eager*. For Transformer baselines, we employ ModernBERT and NeoBERT as representative encoders, especially since they were both recently modernized and optimized using FlashAttention (Dao et al., 2022), RoPE positional encoding (Su et al., 2021), and several other engineering techniques (see Section 2).

RoPE enables evaluation beyond a model's pre-trained context window, which we leverage to measure throughput and latency for ModernBERT and NeoBERT at long sequence lengths. Although such extrapolation may degrade task effectiveness, this does not impact our study, as we are concerned solely with efficiency rather than model quality. In contrast, Avey does not face this limitation because its architecture decouples context width from sequence length, allowing Avey-B to operate at arbitrarily long sequences *without* any additional pre-training. Accordingly, we extend sequence length as needed and compare Avey-B *base* against ModernBERT *base* and NeoBERT *medium* (the only publicly available variant), reporting throughput in this section and latency in Appendix I. The qualitative conclusions presented in this section, however, apply to both throughput and latency.

For ModernBERT and NeoBERT, we also report throughput under both optimized and unoptimized settings, corresponding to execution *with* and *without* FlashAttention. We refer to these configurations as *sys-optimized* and *sys-unoptimized*, respectively. As shown in Fig. 2, the throughput curves for all encoders across sequence lengths from 128 to 96k tokens and under both settings exhibit a consistent structure. In particular, throughput increases at short sequences, plateaus at

medium lengths, and eventually declines as sequence lengths grow large. This behavior follows from the fixed batch size of eight used in our study. To elaborate, each forward pass incurs a constant memory-loading overhead, which dominates when few tokens are processed, leading to low GPU utilization. As sequence length increases, more tokens are processed per batch, amortizing this communication cost and improving utilization. At sufficiently large sequence lengths, however, computation becomes the dominant bottleneck due to arithmetic intensity, memory-bandwidth saturation, and large intermediate activations, causing throughput to decline.

Despite sharing this qualitative profile, the encoders differ markedly in their quantitative scaling. We characterize long-context throughput using a power-law decay model, $T(N) \propto N^{-\alpha}$, where N denotes the sequence length and smaller exponents α indicate better long-context efficiency. Under optimized settings (see Fig. 2 (a)), ModernBERT-sys-optimized and NeoBERT-sys-optimized demonstrate decay exponents of $\alpha_{\text{ModernBERT}} = 0.77$ and $\alpha_{\text{NeoBERT}} = 0.81$, respectively, consistent with the bandwidth- and memory-driven limitations inherent to quadratic self-attention. In contrast, Avey-B-torch-compile displays a substantially milder decay with exponent $\alpha_{\text{Avey-B}} = 0.44$, sustaining significantly higher throughput across the long-context regime.

The unoptimized measurements further accentuate these differences (see Fig. 2 (b)). ModernBERT-sys-unoptimized and NeoBERT-sys-unoptimized exhibit considerably steeper decay, with exponents $\alpha_{\text{ModernBERT}} = 1.03$ and $\alpha_{\text{NeoBERT}} = 1.30$, and both encounter out-of-memory failures well before the maximum tested sequence length. Conversely, Avey-B-eager again achieves the mildest decay, with $\alpha_{\text{Avey-B}} = 0.33$, and maintains stable throughput across the entire sequence-length range. These results indicate that Avey-B's scaling advantage is structural rather than an artifact of kernel-level or compiler optimizations. Specifically, its neural processor is inherently less sensitive to sequence length because computation depends on the fixed split size S, not the full sequence length N. With N/S splits, the total processing cost is $(N/S) \times S^2 = NS = \mathcal{O}(N)$, yielding linear scaling in N and a growing throughput advantage at long contexts, while still being the fastest tested encoder at short contexts.

6 Conclusion

In this paper, we presented Avey-B, a bidirectional encoder built on Avey, a new attention-free foundation model. Avey-B contributes three architectural innovations: (1) decoupling static and dynamic parameterizations, (2) row-normalized similarity in the dynamic layers, and (2) a neural compression module for improving effectiveness and efficiency. Results show that Avey-B delivers consistent gains over Transformer-based encoders, including BERT, RoBERTa, ModernBERT, and NeoBERT on token classification and information retrieval, while outperforming BERT and NeoBERT on every evaluated benchmark. These findings entail that attention might not be the only viable route to strong bidirectional encoders and motivate further study of retrieval-conditioned, non-attention architectures.

7 Reproducibility

All results reported in this paper are reproducible. Section 4 specifies Avey-B's components in detail. The full experimental methodology is provided in Section 5.1 and Appendix B. We attach a repository with code as supplementary material. The repository includes: (1) training, fine-tuning, and evaluation scripts; (2) configuration files with the exact hyperparameters used for every experiment; (3) data preprocessing instructions and dataset references/splits; and (4) environment specifications and run scripts to regenerate all tables and figures. Using the provided commands on hardware comparable to our setup reproduces the reported numbers within expected seed variance.

References

answerdotai-base. Modernbert-base. `https://huggingface.co/answerdotai/ModernBERT-base`. Hugging Face model repository.

answerdotai-large. Modernbert-large. `https://huggingface.co/answerdotai/ModernBERT-large`. Hugging Face model repository.

Payal Bajaj, Daniel Campos, Nick Craswell, Li Deng, Jianfeng Gao, Xiaodong Liu, Rangan Majumder, Andrew McNamara, Bhaskar Mitra, Tri Nguyen, et al. Ms marco: A human generated machine reading comprehension dataset. *arXiv preprint arXiv:1611.09268*, 2016.

Samuel R. Bowman, Gabor Angeli, Christopher Potts, and Christopher D. Manning. A large annotated corpus for learning natural language inference. In *Proceedings of the 2015 Conference on Empirical Methods in Natural Language Processing (EMNLP)*, 2015.

Lola Le Breton, Quentin Fournier, Mariam El Mezouar, John X. Morris, and Sarath Chandar. Neobert: A next-generation bert. *arXiv preprint arXiv:2502.19587*, 2025.

chandar-lab. Neobert. `https://huggingface.co/chandar-lab/NeoBERT`. Hugging Face model repository.

Krzysztof Choromanski, Valerii Likhosherstov, David Dohan, Xingyou Song, Andreea Gane, Tamás Sarlós, Peter Hawkins, Jared Davis, Afroz Mohiuddin, Łukasz Kaiser, David Belanger, Lucy Colwell, and Adrian Weller. Rethinking attention with performers. In *International Conference on Learning Representations (ICLR)*, 2021.

Tri Dao, Daniel Y. Fu, Stefano Ermon, Atri Rudra, and Christopher Ré. Flashattention: Fast and memory-efficient exact attention with io-awareness. In *Advances in Neural Information Processing Systems (NeurIPS)*, 2022.

Yann N. Dauphin, Angela Fan, Michael Auli, and David Grangier. Language modeling with gated convolutional networks. In *Proceedings of the 34th International Conference on Machine Learning (ICML)*, pp. 933–941. PMLR, 2017.

Jacob Devlin, Ming-Wei Chang, Kenton Lee, and Kristina Toutanova. Bert: Pre-training of deep bidirectional transformers for language understanding. *arXiv preprint arXiv:1810.04805*, 2019.

facebook-roberta-base. Roberta base (roberta-base). `https://huggingface.co/FacebookAI/roberta-base`. Hugging Face model repository.

facebook-roberta-large. Roberta large (roberta-large). `https://huggingface.co/FacebookAI/roberta-large`. Hugging Face model repository.

Daniel Y. Fu, Tri Dao, Khaled K. Saab, Armin W. Thomas, Atri Rudra, and Christopher Ré. Hungry hungry hippos: Towards language modeling with state space models. *arXiv preprint arXiv:2212.14052*, 2022.

Hippolyte Gisserot-Boukhlef, Nicolas Boizard, Manuel Faysse, Duarte M Alves, Emmanuel Malherbe, André FT Martins, Céline Hudelot, and Pierre Colombo. Should we still pretrain encoders with masked language modeling? *arXiv preprint arXiv:2507.00994*, 2025.

google-bert-base. Bert base uncased (bert-base-uncased). `https://huggingface.co/google-bert/bert-base-uncased`. Hugging Face model repository.

google-bert-large. Bert large uncased (bert-large-uncased). `https://huggingface.co/google-bert/bert-large-uncased`. Hugging Face model repository.

Albert Gu and Tri Dao. Mamba: Linear-time sequence modeling with selective state spaces. *arXiv preprint arXiv:2312.00752*, 2023.

Albert Gu, Karan Goel, and Christopher Ré. Efficiently modeling long sequences with structured state spaces. In *Advances in Neural Information Processing Systems (NeurIPS)*, 2021.

Weiwei Guo, Xiaowei Liu, Sida Wang, Huiji Gao, Ananth Sankar, Zimeng Yang, Qi Guo, Liang Zhang, Bo Long, Bee-Chung Chen, and Deepak Agarwal. Detext: A deep text ranking framework with BERT. In *Proceedings of the 29th ACM International Conference on Information and Knowledge Management (CIKM '20)*, Virtual Event, Ireland, 2020. ACM. URL `https://arxiv.org/abs/2008.02460`.

Ankit Gupta, Albert Gu, and Jonathan Berant. Diagonal state spaces are as effective as structured state spaces. In *Advances in Neural Information Processing Systems (NeurIPS)*, 2022.

Mohammad Hammoud and Devang Acharya. Don't pay attention. *arXiv preprint arXiv:2506.11305*, 2025.

Pengcheng He, Jianfeng Gao, and Weizhu Chen. Debertav2: Further improving deberta using knowledge distillation. *arXiv preprint arXiv:2111.09543*, 2021a.

Pengcheng He, Xiaodong Liu, Jianfeng Gao, and Weizhu Chen. Deberta: Decoding-enhanced bert with disentangled attention. In *International Conference on Learning Representations (ICLR)*, 2021b.

Pengcheng He, Jianfeng Gao, and Weizhu Chen. Debertav3: Improving deberta using electra-style pre-training with gradient-disentangled embedding sharing. *arXiv preprint arXiv:2111.09543*, 2023.

Eduard Hovy, Mitch Marcus, Martha Palmer, Lance Ramshaw, and Ralph Weischedel. Ontonotes: the 90% solution. In *Proceedings of the human language technology conference of the NAACL, Companion Volume: Short Papers*, pp. 57–60, 2006.

Hugging Face. Fineweb dataset. `https://huggingface.co/datasets/HuggingFaceFW/fineweb`, 2023. Accessed: 2025-04-19.

Xiaoqi Jiao, Yichun Yin, Lifeng Shang, Xin Jiang, Xiao Chen, Linlin Li, Fang Wang, and Qun Liu. Tinybert: Distilling bert for natural language understanding. In *Findings of the Association for Computational Linguistics: EMNLP 2020*, pp. 4163–4174, 2020.

Andrej Karpathy. The most dramatic optimization to nanogpt so far (˜25% speedup) is to simply increase vocab size from 50257 to 50304 (nearest multiple of 64). `https://x.com/karpathy/status/1621578354024677377`, February 2023. X (formerly Twitter) post.

Vladimir Karpukhin, Barlas Oguz, Sewon Min, Patrick Lewis, Ledell Wu, Sergey Edunov, Danqi Chen, and Wen-tau Yih. Dense passage retrieval for open-domain question answering. In *Proceedings of the 2020 Conference on Empirical Methods in Natural Language Processing (EMNLP)*, pp. 6769–6781, 2020.

Angelos Katharopoulos, Apoorv Vyas, Nikolaos Pappas, and François Fleuret. Transformers are rnns: Fast autoregressive transformers with linear attention. In *Proceedings of the 37th International Conference on Machine Learning (ICML)*, 2020.

Omar Khattab and Matei Zaharia. Colbert: Efficient and effective passage search via contextualized late interaction over bert. In *Proceedings of the 43rd International ACM SIGIR Conference on Research and Development in Information Retrieval (SIGIR)*, pp. 39–48, 2020.

Tom Kwiatkowski, Jennimaria Palomaki, Olivia Redfield, Michael Collins, Ankur Parikh, Chris Alberti, Danielle Epstein, Illia Polosukhin, Jacob Devlin, Kenton Lee, et al. Natural questions: a benchmark for question answering research. *Transactions of the Association for Computational Linguistics*, 7:453–466, 2019.

Guokun Lai, Qizhe Xie, Hanxiao Liu, Yiming Yang, and Eduard Hovy. Race: Large-scale reading comprehension dataset from examinations. In *Proceedings of the 2017 Conference on Empirical Methods in Natural Language Processing (EMNLP)*, pp. 785–794. Association for Computational Linguistics, 2017.

Zhenzhong Lan, Mingda Chen, Sebastian Goodman, Kevin Gimpel, Piyush Sharma, and Radu Soricut. Albert: A lite bert for self-supervised learning of language representations. In *International Conference on Learning Representations (ICLR)*, 2020.

Shen Li, Yanli Zhao, Rohan Varma, Omkar Salpekar, Pieter Noordhuis, Teng Li, Adam Paszke, Jeff Smith, Brian Vaughan, Pritam Damania, and Soumith Chintala. Pytorch distributed: Experiences on accelerating data parallel training. *Proceedings of the VLDB Endowment (PVLDB)*, 13 (12):3005–3018, 2020. doi: 10.14778/3407790.3407832. URL `https://www.vldb.org/pvldb/vol13/p3005-li.pdf`.

Hanxiao Liu, Zihang Dai, David So, and Quoc V Le. Pay attention to mlps. *Advances in neural information processing systems*, 34:9204–9215, 2021.

Yinhan Liu, Myle Ott, Naman Goyal, Jingfei Du, Mandar Joshi, Danqi Chen, Omer Levy, Mike Lewis, Luke Zettlemoyer, and Veselin Stoyanov. Roberta: A robustly optimized bert pretraining approach. *arXiv preprint arXiv:1907.11692*, 2019.

Stephen Mayhew, Terra Blevins, Shuheng Liu, Marek Šuppa, Hila Gonen, Joseph Marvin Imperial, Börje F Karlsson, Peiqin Lin, Nikola Ljubešić, Lester James Miranda, et al. Universal ner: A gold-standard multilingual named entity recognition benchmark. *arXiv preprint arXiv:2311.09122*, 2023.

Niklas Muennighoff, Nouamane Tazi, Loïc Magne, Nils Reimers, Douwe Kiela, and Timo Schick. Mteb: Massive text embedding benchmark. *arXiv preprint arXiv:2307.16645*, 2023.

Multi-Linguality Multi-Functionality Multi-Granularity. M3-embedding: Multi-linguality, multi-functionality, multi-granularity text embeddings through self-knowledge distillation, 2024.

Tsendsuren Munkhdalai, Lingkai Kong, Tianxiao Zhang, and Jiawei Han. Infini-attention: Long-context attention in infinite sequence. *arXiv preprint arXiv:2404.07143*, 2024.

Zach Nussbaum, John X Morris, Brandon Duderstadt, and Andriy Mulyar. Nomic embed: Training a reproducible long context text embedder. *arXiv preprint arXiv:2402.01613*, 2024.

OpenAI. How to count tokens with tiktoken. `https://cookbook.openai.com/examples/how_to_count_tokens_with_tiktoken`, 2022. Accessed 2025-09-21.

OpenAI. tiktoken: A fast BPE tokenizer for use with openai models. `https://github.com/openai/tiktoken`, 2025. Accessed 2025-09-21.

Antonio Orvieto and Robert Gower. In search of adam's secret sauce. *arXiv preprint arXiv:2505.21829*, May 2025. doi: 10.48550/arXiv.2505.21829. URL `https://arxiv.org/abs/2505.21829`.

Adam Paszke, Sam Gross, Francisco Massa, Adam Lerer, James Bradbury, Gregory Chanan, Trevor Killeen, Zeming Lin, Natalia Gimelshein, Luca Antiga, Alban Desmaison, Andreas Köpf, Edward Yang, Zach DeVito, Martin Raison, Alykhan Tejani, Sasank Chilamkurthy, Benoit Steiner, Lu Fang, Junjie Bai, and Soumith Chintala. Pytorch: An imperative style, high-performance deep learning library. In *Advances in Neural Information Processing Systems (NeurIPS)*, 2019. URL `https://arxiv.org/abs/1912.01703`.

Bo Peng, Ruichong Zhang, Daniel Goldstein, Eric Alcaide, Xingjian Du, Haowen Hou, Jiaju Lin, Jiaxing Liu, Janna Lu, William Merrill, et al. Rwkv-7" goose" with expressive dynamic state evolution. *arXiv preprint arXiv:2503.14456*, 2025.

Jacob Portes, Alex Trott, Sam Havens, Daniel King, Abhinav Venigalla, Moin Nadeem, Nikhil Sardana, Daya Khudia, and Jonathan Frankle. Mosaicbert: A bidirectional encoder optimized for fast pretraining. *arXiv preprint arXiv:2312.17482*, 2023. doi: 10.48550/arXiv.2312.17482.

Ofir Press, Noah A. Smith, and Mike Lewis. Train short, test long: Attention with linear biases (alibi) enables input length extrapolation. *arXiv preprint arXiv:2108.12409*, 2022.

Alec Radford, Karthik Narasimhan, Tim Salimans, and Ilya Sutskever. Improving language understanding by generative pre-training. OpenAI technical report, 2018. `https://cdn.openai.com/research-covers/language-unsupervised/language_understanding_paper.pdf`.

Alec Radford, Jong Wook Kim, Chris Hallacy, Aditya Ramesh, Gabriel Goh, Sandhini Agarwal, Girish Sastry, Amanda Askell, Pamila Mishkin, Jack Clark, Gretchen Krueger, and Ilya Sutskever. Learning transferable visual models from natural language supervision. In *Proceedings of the 38th International Conference on Machine Learning (ICML)*, 2021.

Prabhakar Raghavan. How ai is powering a more helpful google, October 2020. URL `https://blog.google/products/search/search-on/`. The Keyword (Google). "BERT is now used in almost every query in English." Accessed 2025-09-24.

Pranav Rajpurkar, Jian Zhang, Konstantin Lopyrev, and Percy Liang. Squad: 100,000+ questions for machine comprehension of text. In *Proceedings of the 2016 Conference on Empirical Methods in Natural Language Processing (EMNLP)*, 2016.

Pranav Rajpurkar, Robin Jia, and Percy Liang. Know what you don't know: Unanswerable questions for squad. In *Proceedings of the 56th Annual Meeting of the Association for Computational Linguistics (ACL)*, pp. 784–789, 2018.

Erik F Sang and Fien De Meulder. Introduction to the conll-2003 shared task: Language-independent named entity recognition. *arXiv preprint cs/0306050*, 2003.

Victor Sanh, Lysandre Debut, Julien Chaumond, and Thomas Wolf. Distilbert, a distilled version of bert: smaller, faster, cheaper and lighter. *arXiv preprint arXiv:1910.01108*, 2019.

Keshav Santhanam, Omar Khattab, Christopher Potts, and Matei Zaharia. Colbertv2: Effective and efficient retrieval via lightweight late interaction. *arXiv preprint arXiv:2112.01488*, 2022.

Noam Shazeer. Glu variants improve transformer. *arXiv preprint arXiv:2002.05202*, 2020.

Richard Socher, Alex Perelygin, Jean Wu, Jason Chuang, Christopher D Manning, Andrew Y Ng, and Christopher Potts. Recursive deep models for semantic compositionality over a sentiment treebank. In *Proceedings of the 2013 conference on empirical methods in natural language processing*, pp. 1631–1642, 2013.

Jianlin Su, Yu Lu, Shengfeng Pan, Ahmed Murtadha, Bo Wen, and Yunfeng Liu. Roformer: Enhanced transformer with rotary position embedding. *arXiv preprint arXiv:2104.09864*, 2021.

Yuxuan Su, Xinglin Wang, Yihan Wang, Dong Yu, Yiming Chen, Jing Lin, Tianyu Liu, Zheng Liu, Yu Chen, et al. Gte: General text embeddings with weak supervision. *arXiv preprint arXiv:2308.03281*, 2023.

Zhiqing Sun, Hongkun Yu, Xiaodan Song, Renjie Liu, Yiming Yang, and Denny Zhou. Mobilebert: a compact task-agnostic bert for resource-limited devices. In *Proceedings of the 58th Annual Meeting of the Association for Computational Linguistics (ACL)*, pp. 2158–2170, 2020.

Yi Tay, Mostafa Dehghani, Dara Bahri, and Donald Metzler. Efficient transformers: A survey. *ACM Computing Surveys*, 55(6):1–28, 2022.

Nandan Thakur, Nils Reimers, Johannes Daxenberger, James Cohen, and Iryna Gurevych. Beir: A heterogeneous benchmark for zero-shot evaluation of information retrieval models. In *Proceedings of the 43rd International ACM SIGIR Conference on Research and Development in Information Retrieval (SIGIR)*, pp. 2325–2331, 2021.

Ashish Vaswani, Noam Shazeer, Niki Parmar, Jakob Uszkoreit, Llion Jones, Aidan N. Gomez, Łukasz Kaiser, and Illia Polosukhin. Attention is all you need. In *Advances in Neural Information Processing Systems (NeurIPS)*, 2017.

Alex Wang, Yada Pruksachatkun, Nikita Nangia, Amanpreet Singh, Julian Michael, Felix Hill, Omer Levy, and Samuel R. Bowman. Superglue: A stickier benchmark for general-purpose language understanding systems. In *Advances in Neural Information Processing Systems (NeurIPS)*, 2019a.

Alex Wang, Amanpreet Singh, Julian Michael, Felix Hill, Omer Levy, and Samuel R. Bowman. Glue: A multi-task benchmark and analysis platform for natural language understanding. In *Proceedings of the International Conference on Learning Representations (ICLR)*, 2019b. `https://gluebenchmark.com/`.

Sheng Wang, Ming Zhao, Nguyen Bach, Tao Xu, Zhe Huang, Fei Wu, Tong Wang, Shuo Si, Zhongqiang Li, et al. Text embeddings by weakly-supervised contrastive pre-training. *arXiv preprint arXiv:2212.03533*, 2022.

Zhiguo Wang, Wael Hamza, and Radu Florian. Bilateral multi-perspective matching for natural language sentences. *arXiv preprint arXiv:1702.03814*, 2017.

Benjamin Warner, Antoine Chaffin, Benjamin Clavié, Orion Weller, Oskar Hallström, Said Taghadouini, Alexis Gallagher, Raja Biswas, Faisal Ladhak, Tom Aarsen, Griffin Thomas Adams, Jeremy Howard, and Iacopo Poli. Smarter, better, faster, longer: A modern bidirectional encoder for fast, memory efficient, and long context finetuning and inference. In *Proceedings of the 63rd Annual Meeting of the Association for Computational Linguistics (Volume 1: Long Papers)*, pp. 2526–2547, Vienna, Austria, July 2025. Association for Computational Linguistics. ISBN 979-8-89176-251-0. doi: 10.18653/v1/2025.acl-long.127. URL https://aclanthology.org/2025.acl-long.127/.

Adina Williams, Nikita Nangia, and Samuel R. Bowman. A broad-coverage challenge corpus for sentence understanding through inference. In *Proceedings of the 2018 Conference of the North American Chapter of the Association for Computational Linguistics (NAACL-HLT)*, 2018.

Mitchell Wortsman, Peter J Liu, Lechao Xiao, Katie E Everett, Alexander A Alemi, Ben Adlam, John D Co-Reyes, Izzeddin Gur, Abhishek Kumar, Roman Novak, Jeffrey Pennington, Jascha Sohl-Dickstein, Kelvin Xu, Jaehoon Lee, Justin Gilmer, and Simon Kornblith. Small-scale proxies for large-scale transformer training instabilities. In *The Twelfth International Conference on Learning Representations (ICLR 2024)*, 2024. URL https://openreview.net/forum?id=d8w0pmvXbZ. Oral.

Lee Xiong, Chenyan Xiong, Ye Li, Kwok-Fung Tang, Jina Mao, Paul N. Bennett, Jiadong Chen, and Arnold Overwijk. Approximate nearest neighbor negative contrastive learning for dense text retrieval. In *Proceedings of the International Conference on Learning Representations (ICLR)*, 2021.

Biao Zhang and Rico Sennrich. Root mean square layer normalization. In *Advances in Neural Information Processing Systems (NeurIPS)*, 2019.

Jeffrey Zhu. Bing delivers its largest improvement in search experience using azure gpus, November 2019. URL https://azure.microsoft.com/en-us/blog/bing-delivers-its-largest-improvement-in-search-experience-using-azure-gpus/. Reports serving >1M BERT inferences/sec worldwide. Accessed 2025-09-24.

A Monotonicity Under Decoupling

In Section 4.2, we claimed that decoupling static and dynamic layers maintains *monotonicity with respect to relevance* within each dynamic layer, and that this guarantee is isolated from what a subsequent static layer does. We now formalize and prove this claim.

Setup 1 (dynamic layer). As defined in Section 4.2, given $\mathbf{Z}_{\mathrm{tr}} \in \mathbb{R}^{C\times d'}$ and fixing a target embedding (row) i, Avey-B's dynamic layer computes:

$$\mathbf{S} = \mathcal{N}(\mathbf{Z}_{\mathrm{tr}})\,\mathcal{N}(\mathbf{Z}_{\mathrm{tr}})^{\top}, \tag{9a}$$

$$\widetilde{\mathbf{S}}_{i,j} = \frac{\mathbf{S}_{i,j}}{\sum_{j'=1}^{C} \mathbf{S}_{i,j'} + \varepsilon}, \tag{9b}$$

$$\mathbf{c}_{\mathrm{dyn},i} = \sigma\left(\sum_{j=1}^{C} \widetilde{\mathbf{S}}_{i,j}\,\mathbf{Z}_{\mathrm{tr},j} + \mathbf{b}_i^{(d)}\right), \tag{9c}$$

where $\mathcal{N}(\cdot)$ is per-row ℓ_2 normalization (so $\mathbf{S}$ contains cosine similarities), $\varepsilon > 0$ is a stabilizer, σ is a pointwise monotone activation, and $\mathbf{b}^{(d)}$ is an optional bias.

Assumptions. We assume the following:

(A1) Nonnegative similarities. The enricher uses a nonnegative pointwise activation, namely, ReLU^2 (Hammoud & Acharya, 2025), hence, rows of $\mathcal{N}(\mathbf{Z}_{\mathrm{tr}})$ are nonnegative, implying $\mathbf{S}_{i,j} \geq 0$.

(A2) Positive normalization. For each row i, $\sum_{j=1}^{C} \mathbf{S}_{i,j} + \varepsilon > 0$ with $\varepsilon > 0$.

(A3) Monotone activation. σ is monotone nondecreasing (e.g., Avey-B uses ReLU in Equation 9c).

Proposition A.1 (dynamic layer monotonicity)**.** For a fixed target row i and any two embeddings $j_1, j_2 \in \{1, \ldots, C\}$:

(i) Order preservation. If $\mathbf{S}_{i,j_1} \geq \mathbf{S}_{i,j_2}$ then $\widetilde{\mathbf{S}}_{i,j_1} \geq \widetilde{\mathbf{S}}_{i,j_2}$.

(ii) Self-monotonicity. Increasing $\mathbf{S}_{i,j}$ (while holding $\{\mathbf{S}_{i,k}\}_{k \neq j}$ fixed) weakly increases $\widetilde{\mathbf{S}}_{i,j}$ and does not increase $\widetilde{\mathbf{S}}_{i,k}$ for $k \neq j$.

Consequently, a more relevant token (higher similarity) receives at least as large (and typically larger) weight than a less relevant token, and increasing its relevance cannot reduce or flip the sign of its contribution in the update within the dynamic layer (i.e., the update is monotone with respect to relevance).

Proof. Let $d_i = \sum_{j=1}^{C} \mathbf{S}_{i,j} + \varepsilon$; by **(A2)**, $d_i > 0$. Since $\widetilde{\mathbf{S}}_{i,j} = \mathbf{S}_{i,j}/d_i$ for fixed i, dividing by a positive constant preserves order. In addition, treating d_i as a function of $\mathbf{S}_{i,\cdot}$ and using **(A1)**:

$$\frac{\partial \widetilde{\mathbf{S}}_{i,j}}{\partial \mathbf{S}_{i,j}} = \frac{d_i - \mathbf{S}_{i,j}}{d_i^2} \;\geq\; 0, \qquad \text{since } d_i \geq \mathbf{S}_{i,j} \text{ by } \textbf{(A1)} \text{ and } \varepsilon > 0, \tag{10a}$$

$$\frac{\partial \widetilde{\mathbf{S}}_{i,k}}{\partial \mathbf{S}_{i,j}} = -\frac{\mathbf{S}_{i,k}}{d_i^2} \;\leq\; 0, \qquad k \neq j, \qquad \text{by } \textbf{(A1)}. \tag{10b}$$

Thus, increasing a token's similarity weakly increases (or cannot reduce) its own normalized weight (by Equation 10a) and weakly decreases (or does not increase) others' (by Equation 10b). By **(A1)**, $\widetilde{\mathbf{S}}_{i,j} \geq 0$, so each token's influence enters the pre-activation with a nonnegative coefficient; by **(A3)**, σ cannot invert these contributions. Hence, the dynamic update is monotone with respect to relevance. ■

Setup 2 (static layer). Consider a dynamic layer at depth ℓ followed by a static layer:

$$\mathbf{h}^{(\ell+1)} = \sigma\big(\, \widetilde{\mathbf{S}}^{(\ell)}\, \mathbf{Z}_{\mathrm{tr}}^{(\ell)} + \mathbf{b}^{(d)}\big), \tag{11}$$

$$\mathbf{y}^{(\ell+2)} = \sigma\big(\, \mathbf{V}\, \mathbf{h}^{(\ell+1)} + \mathbf{b}^{(s)}\big), \tag{12}$$

where $(\mathbf{V}, \mathbf{b}^{(s)})$ are learned parameters that do not depend on $\mathbf{S}^{(\ell)}$ or $\widetilde{\mathbf{S}}^{(\ell)}$.

Proposition A.2 (static layer non-violation)**.** A static layer (as in equation 12) cannot violate the monotonicity guarantee of Proposition A.1 established for a preceding dynamic layer (as in Equation 11) at depth ℓ.

Proof. The monotonicity statements in Proposition A.1 concern only the relationship between the relevance scores $\mathbf{S}^{(\ell)}$ and the normalized scores $\widetilde{\mathbf{S}}^{(\ell)}$ used *inside* the dynamic update equation 11. The static map $\mathbf{h}^{(\ell+1)} \mapsto \mathbf{y}^{(\ell+2)}$ depends on $\mathbf{h}^{(\ell+1)}$ and the similarity-agnostic parameters $(\mathbf{V}, \mathbf{b}^{(s)})$; it neither accesses nor alters $\mathbf{S}^{(\ell)}$ or $\widetilde{\mathbf{S}}^{(\ell)}$. Therefore, composing the dynamic update with a static layer cannot change the inequalities and partial orders that define monotonicity for the dynamic layer's scores. ■

Remark. A static layer reshapes representations that subsequent dynamic layers will use to compute new similarities, but it does not retroactively modify the scores already assigned by a preceding dynamic layer. Thus, monotonicity holds at each dynamic layer, and decoupling preserves this guarantee throughout the stack.

Table 3: A comparison of all the evaluated encoders across different dimensions.

Dimension	BERT		RoBERTa		ModernBERT		NeoBERT	Avey-B	
	base	*large*	*base*	*large*	*base*	*large*	*medium*	*base*	*large*
Parameters	120M	350M	125M	355M	149M	395M	250M	165M	391M
Data Sources	BooksCorpus Wikipedia		BooksCorpus OpenWebText Stories / CC-News		Undisclosed		RefinedWeb	FineWeb	
Pre-training Context Width	512		512		$1{,}024 \rightarrow 8{,}192$		$1{,}024 \rightarrow 4{,}096$	2,048	
Inference Sequence Length	512		512		8,192		4,096	∞	
Masking Rate	15%		15%		30%		20%	20%	
Masking Scheme	80/10/10		80/10/10		–		100	100	
Tokens Seen	131B		131B		$\sim$2T		2.1T	180B	

B Pretraining Methodology

In this section, we detail the pretraining setup. For Avey-B, we adopt the same tokenizer as Avey (Hammoud & Acharya, 2025), namely, a BPE tokenizer derived from OpenAI's `p50k_base` (OpenAI, 2022; 2025), with the vocabulary size set to 50,304 to align with multiple-of-64 boundaries and improve hardware efficiency (Karpathy, 2023). We retain BERT-style special tokens for backward compatibility with downstream applications, while using only the `[MASK]` token during pre-training.

We pretrain two Avey-B sizes, *base* (165M) and *large* (391M), for 180B tokens drawn from the FineWeb 300BT split (Hugging Face, 2023), using PyTorch DDP across 16 NVIDIA H200 GPUs (Paszke et al., 2019; Li et al., 2020). The global batch size is set to 512K tokens for both models and we utilize the AdamW optimizer with $\beta_1 = \beta_2 = 0.95$ (Orvieto & Gower, 2025), $\epsilon = 10^{-18}$ (Wortsman et al., 2024), weight decay of 0.01, and gradient clipping at 1.0. For the learning-rate schedule, we employ a 10% linear warmup to 5×10^{-4} (base) or 2.5×10^{-4} (large), followed by cosine decay to zero over the remaining 90% of steps.

For ablations and design–choice studies, we use the Avey-B *base* model, pretrained with a constant learning rate of 10^{-3} for 10B tokens. During pretraining, sequences are *packed* so that each training example meets the target sequence length, following the original Avey setup. We train with a masked language modeling (MLM) objective, randomly masking 20% of tokens per example after exploring several masking rates (see Appendix G).

Finally, for the Transformer-based encoders, we use publicly available pretrained checkpoints from the Hugging Face Hub (google-bert-base; google-bert-large; facebook-roberta-base; facebook-roberta-large; answerdotai-base; answerdotai-large; chandar-lab). Table 3 summarizes the evaluated models along key dimensions, including parameter count, context window, and pretraining tokens, among others.

C Should the ranker operate bidirectionally?

In the original, unidirectional Avey architecture, the ranker attends only to *preceding* splits (left context) to preserve the causal constraint of autoregressive modeling. With bidirectional Avey-B, we ask whether the ranker should, like the neural processor, operate bidirectionally, retrieving from both left and right contexts of the current split.

To this end, we conduct all our experiments using the Avey-B *base* variant (165M parameters) (see Table 3). We pretrain it on 10B FineWeb (Hugging Face, 2023) tokens with a constant learning rate of 1×10^{-3} and a 20% masking rate. As suggested in Section 5.1, we finetune SC and TC for one epoch, QA for four epochs, and IR for 1,000 optimization steps. For each task, we run 5 independent seeds with a learning rate of 5×10^{-4}, using a 10% warmup followed by linear decay to zero over the remaining 90% of steps. We report the *best-of-5* score for each configuration as an upper bound. Metrics are accuracy for SC, F1 for TC and QA, and NDCG@10 for IR. Table 4 shows all the results.

Table 4: Effectiveness results comparing unidirectional vs. bi-directional rankers.

Ranker Type	SC				TC				QA				IR			
	MNLI	QQP	SST-2	**Avg.**	CONLL	Onto.	UNER	**Avg.**	ReCoRD	SQuAD	SQuADv2	**Avg.**	MLDR	MS MARCO	NQ	**Avg.**
Unidirectional ranker	**81.39**	**88.92**	**91.86**	**87.39**	**92.96**	**93.21**	93.97	**93.38**	**30.22**	**62.26**	**60.72**	**51.07**	**60.27**	**87.48**	**76.71**	**74.82**
Bi-directional ranker	80.54	88.45	91.74	86.91	92.62	92.91	**94.35**	93.29	10.64	45.34	53.56	36.51	60.05	90.02	48.54	66.20

In particular, Table 4 contrasts a *unidirectional* ranker with a *bidirectional* ranker across SC, TC, QA, and IR task categories. As illustrated, the bidirectional ranker consistently underperforms the unidirectional ranker. While the gap is modest on SC ($87.39 \rightarrow 86.91$; $\Delta = -0.48$) and TC ($93.38 \rightarrow 93.29$; $\Delta = -0.09$), it is substantial on QA ($51.07 \rightarrow 36.51$; $\Delta = -14.56$) and IR ($74.82 \rightarrow 66.20$; $\Delta = -8.62$). Notably, QA performance degrades sharply, with F1 of ReCoRD dropping from 30.22 to 10.64, suggesting that right-context retrieval at the split level may severely harm evidence selection for reasoning.

We identify two likely causes for this behavior. First, a unidirectional ranker enforces causal ordering and encourages the model to accumulate evidence along the discourse flow. Natural language often exhibits forward dependencies, whereby content in a later split is best interpreted in light of earlier splits. As such, allowing the current split to pair with future splits can dilute or override strong signals from its relevant preceding splits. Second, Avey-B already provides look-ahead, *token-level* contextualization within each split (the contextualizer operates without a causal mask on each split) so every position in it except the last has access to rightward tokens. Therefore, additional look-ahead, *split-level* contextualization seems often redundant and at times even disruptive.

In summary, these findings suggest that while look-ahead, token-level contextualization within a split benefits Avey-B, look-ahead, split-level contextualization, driven by the ranker attending to both left and right split contexts of the current split, is not advantageous and potentially counterproductive.

D How to Arrange Static and Dynamic Layers?

Decoupling static and dynamic parameterizations into distinct layer types in Avey-B introduces a key architectural degree of freedom, that is, *how to arrange static (S) and dynamic (D) layers across depth*. We therefore evaluate the following families of patterns and report their effectiveness:

1. **Interleaved**: Alternate $S \leftrightarrow D$. With an even number of layers, we test both start points, $S \rightarrow D \rightarrow \cdots$ and $D \rightarrow S \rightarrow \cdots$.
2. **Single dynamic**: Exactly one D and the remainder S, placing D either at the *head* (to prime downstream static transformations) or at the *tail* (to refine final representations).
3. **Two-stage stack**: First half one type and second half the other, considering both orders ($S^{L/2} \rightarrow D^{L/2}$ and $D^{L/2} \rightarrow S^{L/2}$).
4. **Uniform stack**: Either all-static or all-dynamic stack, as boundary conditions.

We utilize the experimental setup described in Appendix C. Table 5 reports all the results across SC, TC, QA, and IR task categories. Two consistent trends emerge. First, the *interleaved* arrangement, $S \rightarrow D \rightarrow \cdots$, attains the strongest average performance on SC, TC, and QA, while remaining competitive on IR. This suggests that a static front layer is potentially providing a stable representational "scaffold" before any input-dependent mixing, reducing variance introduced by raw similarity scores and improving downstream contextualization. Second, the interleaved pattern, $D \rightarrow S \rightarrow \cdots$, underperforms the $S \rightarrow D \rightarrow \cdots$ variant (most notably on QA and IR) likely because early, similarity-driven updates are fragile without a learned (static) basis to shape features prior to dynamic contextualization.

The *uniform stack, all-static* configuration performs worse than interleaved arrangements but only modestly so (it even slightly outperforms them on IR), indicating that static linear projections alone already enable strong contextualization, even without any input-dependent adaptation. Conversely, the *uniform stack, all-dynamic* pattern performs worse across all benchmark categories (particularly QA). The *single-dynamic* and *two-stage stack* arrangements fall between these extremes, though

Table 5: Effectiveness results across different static (S) and dynamic (D) layering patterns.

Pattern	SC				TC				QA				IR			
	MNLI	QQP	SST-2	**Avg.**	CONLL	Onto.	UNER	**Avg.**	ReCoRD	SQuAD	SQuADv2	**Avg.**	MLDR	MS MARCO	NQ	**Avg.**
Interleaved, $S \to D \to \cdots$	**81.39**	**88.92**	**91.86**	**87.39**	**92.96**	**93.21**	93.97	**93.38**	**30.22**	**62.26**	**60.72**	**51.07**	60.27	87.48	76.71	74.82
Interleaved, $D \to S \to \cdots$	77.89	87.51	90.37	85.26	91.73	92.48	93.24	92.48	21.31	56.93	55.77	44.67	52.67	88.47	68.63	69.92
Single dynamic as a head	73.69	86.55	91.06	83.77	92.42	92.75	93.31	92.83	22.42	56.94	54.87	44.74	60.22	**89.70**	73.32	74.41
Single dynamic as a tail	73.19	87.90	91.63	84.24	92.58	93.10	93.80	93.16	24.64	55.29	54.06	44.66	60.55	87.72	75.31	74.53
Two-stage stack, $S^{L/2} \to D^{L/2}$	75.70	86.56	90.25	84.17	92.51	92.65	**94.24**	93.13	15.29	52.18	55.09	40.85	54.97	85.92	67.54	69.48
Two-stage stack, $D^{L/2} \to S^{L/2}$	74.37	87.15	91.17	84.23	92.70	93.03	93.72	93.15	29.30	54.36	51.20	44.95	59.28	89.56	**76.74**	**75.19**
Uniform stack, all-static	77.58	87.97	91.51	85.69	92.66	93.10	94.04	93.27	23.85	56.43	54.73	45.00	**62.54**	86.38	75.92	74.95
Uniform stack, all-dynamic	68.04	83.26	87.27	79.52	90.31	90.86	91.17	90.78	19.49	47.51	50.44	39.15	57.70	89.33	69.50	72.18

Table 6: Effectiveness results across different normalization schemes.

Normalization Scheme	SC				TC				QA				IR			
	MNLI	QQP	SST-2	**Avg.**	CONLL	Onto.	UNER	**Avg.**	ReCoRD	SQuAD	SQuADv2	**Avg.**	MLDR	MS MARCO	NQ	**Avg.**
Divide-by-sum norm	**81.39**	**88.92**	**91.86**	**87.39**	**92.96**	**93.21**	93.97	**93.38**	**30.22**	**62.26**	**60.72**	**51.07**	60.27	87.48	**76.71**	74.82
RMS norm	64.70	87.21	88.76	80.22	90.82	92.12	91.89	91.61	21.37	56.09	56.33	44.60	50.27	89.33	66.68	68.76
Softmax	79.31	88.16	91.06	86.18	92.39	92.96	93.45	92.93	27.70	59.29	58.55	48.51	61.83	**89.75**	74.43	**75.34**
Scaled softmax	76.70	87.24	**91.86**	85.27	92.63	93.02	**94.07**	93.24	24.14	58.79	56.23	46.39	**62.24**	87.63	74.39	74.75

they typically trail the interleaved static-first design (except for two-stage stack, $D^{L/2} \to S^{L/2}$ on IR). Overall, these findings highlight that while dynamic parameterization contributes meaningfully to performance, it is most effective when interleaved with static layers that supply a stable basis and representational depth.

E How to Normalize?

In Avey-B, dynamic layers contextualize tokens by constructing a cosine similarity matrix from pairwise cosine scores of the input. Since the similarity scores are used to perform a weighted sum of input embeddings at every position and the sum of the raw similarity magnitudes can vary significantly, we tested several normalization strategies to stabilize training and improve generalization, including *divide-by-sum norm* (i.e., row-wise normalization by the sum of similarities), *RMS norm* (i.e., row-wise normalization by root mean square), *softmax*, and *scaled softmax* (with temperature scaling, analogous to scaled dot-product attention). In all the tests, we used the same experimental setup discussed in Appendix C.

As shown in Table 6, the simple divide-by-sum norm method achieves the strongest overall performance, outperforming alternatives on SC, TC, and QA, and almost matching or surpassing them on IR. Notably, divide-by-sum norm provides a balanced distribution of contextual weights while retaining sign information, which is lost under softmax-based schemes. By contrast, softmax and scaled softmax yield weaker SC, TC, and QA scores but softmax outperforms divide-by-sum norm on IR. On average, RMS norm underperforms divide-by-sum norm across all categories.

These findings indicate that unlike self-attention, which benefits from exponential normalization (as provided by softmax), Avey-B's cosine-based dynamic layers benefit from a *conservative, structure-preserving* normalization. Exponentiation amplifies outliers, distorts relative similarity ratios, and can swamp the static path. In contrast, *divide-by-sum norm* preserves the ordering and margins of similarities, constrains each row to a convex combination (weights in $[0, 1]$ that sum to 1), and effectively bounds the operator norm, yielding stable gradients and preventing the dynamic stream from overwhelming the static contributions. Empirically, this simple choice delivers strong gains across SC, TC, QA, and IR while maintaining robust training dynamics.

F What are the Best Sequence Length, Split Size, and Top-k Values?

We now analyze how Avey-B's downstream performance is affected by the ranker's three hyperparameters, namely, the training sequence length N, the split size S, and the number of top-k splits selected for contextualization. N governs the size of the candidate pool available to the ranker, S

Table 7: Effectiveness results across different sequence length N, split size S, and top-k values.

N	S	k	SC				TC				QA				IR			
			MNLI	QQP	SST-2	**Avg.**	CONLL	Onto.	UNER	**Avg.**	ReCoRD	SQuAD	SQuADv2	**Avg.**	MLDR	MS MARCO	NQ	**Avg.**
512	128	1	80.09	88.82	91.63	86.85	92.69	**93.08**	**93.85**	**93.21**	27.65	60.44	58.82	48.97	60.06	88.89	76.11	75.02
		3	**80.95**	**88.89**	91.63	**87.16**	**92.74**	93.03	93.55	93.11	28.11	60.66	58.79	49.19	**60.72**	**90.11**	76.06	**75.63**
	256	1	79.68	88.75	**92.32**	86.92	92.27	92.94	93.69	92.97	**43.70**	**71.25**	**64.06**	**59.67**	60.71	88.61	**76.29**	75.20
1024	128	1	**80.79**	88.80	91.63	87.07	92.87	93.03	93.81	93.24	27.42	61.14	58.85	49.14	60.44	88.95	76.05	75.15
		3	80.02	88.71	91.63	86.79	**92.89**	93.06	**94.43**	**93.46**	28.74	61.55	60.49	50.26	61.17	**90.26**	75.66	75.70
		5	80.64	88.62	91.40	86.89	92.86	93.13	93.88	93.29	28.69	61.49	59.79	49.99	61.81	86.86	75.61	74.76
		7	80.70	**89.02**	**91.74**	**87.15**	92.44	93.14	93.83	93.14	27.96	**63.47**	59.98	50.47	**62.58**	86.40	66.73	71.90
	256	1	79.53	88.80	91.28	86.54	92.10	93.02	93.57	92.90	42.82	70.16	62.54	58.51	60.88	88.87	76.34	75.36
		3	79.95	88.65	91.40	86.67	92.10	92.84	93.48	92.81	42.51	70.55	63.16	58.74	59.14	89.43	77.05	75.21
	512	1	79.41	88.35	91.51	86.42	92.65	**93.18**	93.74	93.19	**43.96**	**71.92**	**63.91**	**59.93**	60.26	89.20	**77.82**	**75.76**
2048	128	1	80.60	88.93	91.74	87.09	92.85	93.13	94.05	93.34	28.72	61.50	59.13	49.78	60.21	**90.69**	75.15	75.35
		3	80.94	88.95	91.63	87.17	92.52	93.00	93.68	93.07	28.49	60.95	59.73	49.72	60.71	89.22	75.48	75.14
		5	80.98	88.66	91.51	87.05	92.86	93.17	94.02	93.35	27.07	60.27	59.23	48.86	59.02	88.43	75.73	74.39
		7	67.24	88.42	91.63	82.43	91.77	92.69	93.00	92.49	27.76	61.81	58.45	49.34	57.08	86.89	73.55	72.51
		9	80.64	88.84	91.51	87.00	92.54	92.97	93.82	93.11	29.82	62.44	59.52	50.59	60.77	88.27	75.93	74.99
		11	80.49	88.75	91.97	87.07	92.63	93.05	93.45	93.04	29.54	59.77	57.95	49.09	58.14	89.43	75.54	74.37
		13	**81.14**	88.75	**92.20**	**87.36**	92.92	93.13	94.05	**93.37**	27.36	59.98	58.01	48.45	60.21	90.31	**78.48**	**76.33**
		15	80.78	**89.01**	91.63	87.14	92.51	92.94	**94.11**	93.19	28.27	60.34	59.46	49.36	58.69	88.11	76.03	74.28
	256	1	70.61	88.69	92.09	83.80	92.38	**93.18**	94.02	93.19	44.32	70.96	63.58	59.62	**60.84**	88.15	77.24	75.41
		3	80.18	88.91	91.74	86.94	92.33	93.05	93.75	93.04	42.91	71.99	**64.81**	59.90	60.02	90.36	76.58	75.65
		5	79.45	88.48	90.71	86.21	91.51	92.46	92.77	92.25	38.85	69.88	62.09	56.94	56.72	88.11	73.70	72.84
		7	78.98	88.65	91.74	86.46	**93.00**	92.85	93.66	93.17	42.89	70.64	63.25	58.93	59.42	88.35	76.36	74.71
	512	1	79.37	88.52	91.63	86.51	92.41	92.77	93.26	92.81	41.67	71.45	62.20	58.44	56.76	88.67	77.94	74.46
		3	79.36	88.67	91.28	86.44	92.15	92.87	94.00	93.01	**46.39**	**72.34**	64.06	**60.93**	55.65	87.32	75.89	72.95
	1024	1	75.29	88.34	91.40	85.01	92.10	92.79	93.57	92.82	44.88	70.47	62.05	59.13	55.86	90.07	73.93	73.29

determines the size (in tokens) of each candidate split, and the effective context width seen by the contextualizer is $C = S(k+1)$. We follow the experimental setup described in Appendix C. Table 7 illustrates all the results.

To begin with, the dominant trend across tasks is that performance peaks when the effective context $C = S\,(k{+}1)$ matches or closely approximates the training sequence length N. For example, on QA with $N{=}2048$, the best average occurs at $S{=}512$, $k{=}3$, giving $C{=}512 \times (3{+}1){=}2048{=}N$. For SC, TC, and IR at $N{=}2048$, the strongest averages are at $S{=}128$, $k{=}13$, yielding $C{=}128 \times (13{+}1){=}1792$, close to N. Similar behavior holds for $N{=}512$ and $N{=}1024$ across categories, with one slight exception, that is, TC. In particular, on TC, the best setting often lands on $C \approx N/2$ (e.g., at $N{=}512$ the optimum is $S{=}128$, $k{=}1$, so $C{=}256{=}N/2$, but it is only $+0.1$ points away from the effectiveness at $N{=}512, S = 128, k = 3$, which yields $C{=}128 \times (3{+}1){=}512{=}N$).

In summary, Avey-B's performance generally improves with a larger training sequence length N. In our experiments, the best results occur at the largest tested $N{=}2048$ for SC, QA, and IR. The exception is TC, which peaks at $N{=}512$ but is within $+0.09$ points of the $N{=}1024$ setting. Across these optima, the coverage heuristic $C = S\,(k{+}1) \approx N$ is consistently satisfied (matching or closely approaching N). This pattern suggests that, for a bidirectional encoder, one should enlarge the candidate pool via larger N while ensuring ample contextual coverage by setting $S\,(k{+}1)$ to match or closely track N. Averaging over all task categories, the best overall configuration is $N{=}2048$, $S{=}256$, $k{=}3$, hence, it was adopted as Avey-B's default configuration.

G What is the Best Masking Rate?

Because Avey-B is pretrained with masked language modeling, the fraction of tokens replaced by the `[MASK]` token sets the task difficulty. In particular, too little masking makes reconstruction nearly trivial, whereas too much masking deprives the model of sufficient contextual signal for reliable prediction. To calibrate this trade-off, we swept masking rates from 10% to 50% for both the *base* and *large* models (see Table 3 in Appendix B), while following the same experimental setup described in Appendix C (except for the masking rate since we vary it here).

Table 8: Effectiveness results at different masking rates for Avey-B's *base* model.

Masking %	SC				TC				QA				IR			
	MNLI	QQP	SST-2	**Avg.**	CONLL	Onto.	UNER	**Avg.**	ReCoRD	SQuAD	SQuADv2	**Avg.**	MLDR	MS MARCO	NQ	**Avg.**
10%	78.07	88.02	91.86	85.98	91.61	92.54	93.50	92.55	36.64	68.57	60.65	55.29	51.02	85.75	71.50	69.42
20%	**80.18**	**88.91**	91.74	**86.94**	92.33	**93.05**	**93.75**	93.04	**42.91**	**71.99**	**64.81**	**59.90**	60.02	**90.36**	76.58	75.65
30%	78.62	88.49	**91.97**	86.36	92.45	93.01	**93.75**	**93.07**	42.80	71.26	63.85	59.30	**62.16**	89.72	76.19	76.02
40%	77.05	88.02	91.51	85.53	92.26	92.90	93.49	92.88	39.70	69.84	62.45	57.33	59.67	90.33	74.56	74.85
50%	66.12	88.32	91.06	81.83	**92.86**	92.62	93.16	92.88	42.15	70.44	62.90	58.50	62.03	90.06	**77.69**	**76.59**

Table 9: Effectiveness results at different masking percentages for Avey-B's *large* model.

Masking %	SC				TC				QA				IR			
	MNLI	QQP	SST-2	**Avg.**	CONLL	Onto.	UNER	**Avg.**	ReCoRD	SQuAD	SQuADv2	**Avg.**	MLDR	MS MARCO	NQ	**Avg.**
10%	81.01	88.54	92.09	87.21	92.39	92.91	93.32	92.87	42.46	71.53	64.63	59.54	54.58	88.73	75.25	72.85
20%	**82.12**	89.19	**92.32**	**87.88**	92.76	92.94	93.65	93.12	47.93	72.84	65.79	62.19	63.53	**91.54**	80.47	78.51
30%	81.54	**89.43**	91.74	87.57	92.59	92.98	**93.83**	93.13	**48.16**	**73.44**	**66.52**	**62.71**	61.72	89.31	**81.76**	77.60
40%	70.21	89.11	92.20	83.84	92.51	**93.13**	93.65	93.10	46.29	73.36	65.71	61.79	**64.09**	90.96	81.35	**78.80**
50%	78.19	89.02	92.20	86.47	**92.83**	92.95	**93.83**	**93.20**	46.99	71.28	63.89	60.72	61.63	90.49	79.37	77.16

As shown in Table 8, increasing the masking rate from 10% to 20% improves performance across SC, TC, QA, and IR for the base model. Overall, scores typically peak at around 20%–30% masking, yielding consistent gains on SC, TC, and QA. The exception is IR, which attains its best results at 50% masking. At higher masking levels (40%–50%), performance can drop markedly (e.g., MNLI), indicating that the smaller-capacity model struggles when too little context is visible (masking becomes overly aggressive, weakening both the input signal and the training target).

The larger model is more robust to masking but still follows a similar trend to the base variant (see Table 9). Performance generally improves from 10% to 20–30% masking, which offers the best cross-task trade-off (an exception is TC, which peaks at 50%). QA and IR benefit the most, with ReCoRD, MLDR, and NQ rising by over +5, +9, and +6 points, respectively, relative to 10% masking. Although the large model tolerates 40–50% masking with modest degradation, SC remains sensitive, whereby at 40% masking, MNLI drops by $\sim$12 points versus 20%, then partially recovers at 50%, going up by $\sim$8 points versus 40%. These patterns indicate that overly aggressive masking can destabilize training even at higher capacity.

Overall, both models indicate 20–30% masking as near-optimal, thus, we pretrain both at 20%.

H Ablation Study

In this study, we conduct a series of ablation experiments on Avey-B. To this end, we fix (1) the sequence length N, split size S, and top-k retrieval depth to the best settings from Appendix F; (2) the static–dynamic interleaving pattern to the best arrangement from Appendix D; and (3) the dynamic-layer normalization to the most effective scheme from Appendix E. In addition, we follow the experimental setup described in Appendix C.

Table 10 reports ablations over five key architectural components of Avey-B: (1) decoupling static and dynamic parameterizations; (2) applying row-wise normalization in the dynamic layers; (3) incorporating a neural compressor within the ranker; (4) adding a residual connection between the compressor output and the original tokens of the current split that is being compressed with its top-k retrieved splits; and (5) removing the ranker entirely.

As illustrated in Table 10, coupling the static and dynamic parameterizations (i.e., see "full design" and "w/o decoupling" rows) yields consistent drops of 1.43%, 2.12%, 2.53%, and 7.40% on SC, TC, QA, and IR, respectively, confirming that separating similarity scoring from neural learning improves accuracy. Row-wise normalization proves even more critical, whereby removing it leads to significantly larger degradations of 3.55%, 0.87%, 7.65%, and 15.33% across SC, TC, QA, and IR, respectively.

As discussed in Section 4.3, the neural compressor reduces the number of contextualized tokens per split from $(k{+}1)S$ to S. This reduction yields a substantial $4.37\times$ throughput improvement

Table 10: Ablations of Avey-B, removing one component at a time while holding all others fixed. (1) *w/o normalization*: removes row-wise normalization in the dynamic layers; (2) *w/o decoupling*: reverts to coupled static and dynamic parameterizations; (3) *w/o compression*: omits the neural compressor; (4) *w/o residual*: discards the residual connection between the compressor output and the current split's tokens; and (5) *w/o ranker*: disables the ranker entirely.

Model	SC				TC				QA				IR			
	MNLI	QQP	SST-2	**Avg.**	CONLL	Onto.	UNER	**Avg.**	ReCoRD	SQuAD	SQuAD v2	**Avg.**	MLDR	MS MARCO	NQ	**Avg.**
Avey-B (full design)	80.74	88.91	**91.97**	**87.20**	**91.84**	93.25	**93.09**	**92.72**	39.60	68.52	**60.48**	56.20	57.49	**90.38**	75.64	74.50
Avey-B w/o normalization	77.47	84.60	90.25	84.10	90.98	92.65	92.12	91.91	29.72	67.15	58.83	51.90	46.43	82.89	59.92	63.08
Avey-B w/o decoupling	79.94	88.60	89.33	85.95	89.10	92.11	91.06	90.75	36.86	67.89	59.57	54.77	55.00	82.77	69.18	68.98
Avey-B w/o compression	**80.80**	**89.03**	91.17	87.00	91.52	**93.29**	92.97	92.59	**42.80**	**70.54**	59.77	**57.70**	**60.95**	89.13	**76.92**	**75.66**
Avey-B w/o residual	77.53	87.48	90.37	85.12	90.80	92.44	91.17	91.47	34.71	66.08	56.02	52.27	55.22	86.74	71.72	71.22
Avey-B w/o ranker	77.36	87.32	88.76	84.48	90.20	92.39	90.74	91.11	25.85	66.27	57.92	50.01	38.28	85.35	61.93	61.85

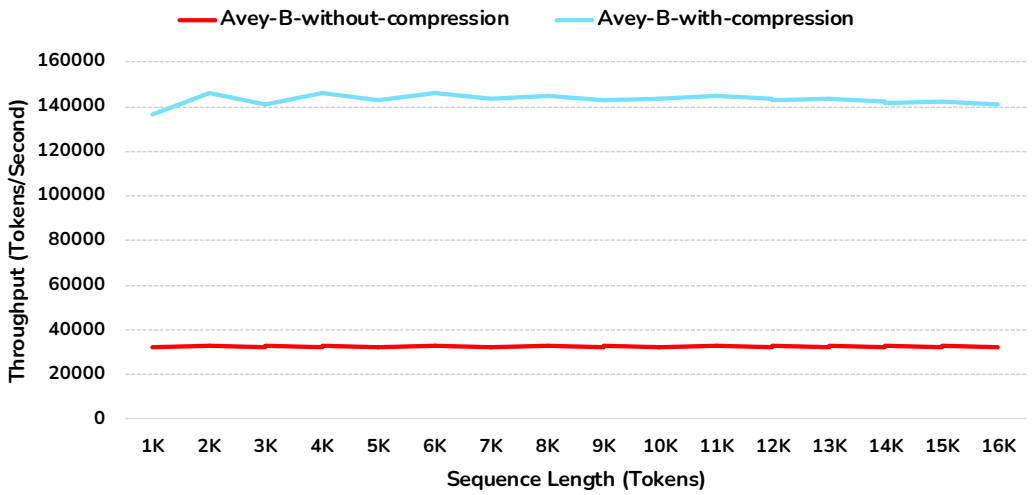

Figure 3: The throughput of Avey-B *with* and *without* the neural compressor.

(see Fig. 3) while preserving strong task performance (see Table 10). On SC and TC, compression has negligible effect and even produces slight average gains of $+0.23\%$ and $+0.14\%$, respectively, likely due to the removal of noisy global tokens that can arise under top-k retrieval[1]. In contrast, QA and IR exhibit modest average drops of 2.68% and 1.56%, respectively. These tasks rely more heavily on fine-grained cross-split evidence and subtle retrieval cues, which compression may partially attenuate. Overall, considering the $4.37\times$ efficiency improvement, the negligible (and sometimes positive) impact on SC and TC, and the modest reductions on QA and IR, the neural compressor provides a clear and favorable efficiency–effectiveness trade-off.

Besides compression, Avey-B adds a residual connection between the compressor output and the current split's S tokens to preserve local signal. Table 10 shows that removing this residual degrades every benchmark, with an average reduction of 3.38%, underscoring its role in maintaining lexical fidelity and stabilizing context integration.

Finally, as described in (Hammoud & Acharya, 2025), the ranker is invoked *only once* per forward/backward pass, prior to the first layer of the neural processor, and retrieves the top-k relevant splits for each current split using shallow (initial) embeddings. One might expect that deeper contextualized embeddings could yield better retrieval; however, removing the ranker entirely (i.e., allowing the neural processor to fit and operate on the entire sequence) results in universal degradation across all benchmarks, with a large average drop of 7.46% (see Table 10). This corroborates that retrieval is essential for Avey-B's effectiveness.

[1]With a split containing S tokens and the absence of a hard relevance threshold (where the ranker retrieves the top-k splits for each query split regardless of their absolute relevance), it is possible for some retrieved splits to contain weakly relevant or noisy tokens.

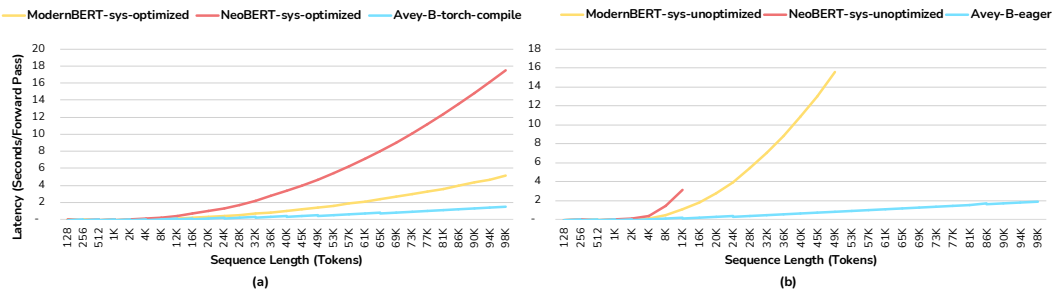

Figure 4: Latency of Avey-B, ModernBERT, and NeoBERT on NVIDIA B200 GPUs with mixed precision (BF16). We use Avey-B *base*, ModernBERT *base*, and NeoBERT *medium* (the only publicly available size). Avey-B is shown in (a) as optimized using `torch.compile` (no fused-kernel implementation is available yet) and in (b) as unoptimized (eager). For ModernBERT and NeoBERT, latency is shown for system–optimized (*with* FlashAttention) and system–unoptimized (eager) variants in (a) and (b), respectively.

Importantly, retrieval based on shallow or static embeddings is a standard practice in dense retrieval and matching systems such as DPR (Karpukhin et al., 2020), ColBERT (Khattab & Zaharia, 2020), ANCE (Xiong et al., 2021), and CLIP (Radford et al., 2021), among others. These systems deliberately rely on early-layer or fixed representations because deeper contextualized embeddings tend to become increasingly task-specific, thereby distorting global semantic structure and degrading their overall retrieval quality.

To evaluate whether deeper-layer retrieval is beneficial, we incorporated the ranker at *every* layer such that it operates on contextualized embeddings. This intervention substantially degraded performance, causing an average drop of 27.28% across benchmarks, and slowed efficiency by $5.9\times$. These findings reinforce that deeper-layer retrieval is not only computationally prohibitive (as it would require recomputing MaxSim and reassembling contextualized blocks at each layer) but also detrimental for effectiveness.

To summarize, these ablations collectively validate Avey-B's core architectural principles, namely, (1) decoupling and normalization are critical for both effectiveness and stability (more on this in Appendix J); (2) the residual connection preserves essential local information; (3) the neural compressor delivers substantial efficiency gains with minimal accuracy loss; and (4) the ranker is indispensable, with shallow-embedding retrieval proving both computationally justified and empirically optimal.

I Latency Results

In Section 5.4, we reported *throughput* (tokens/second) for Avey-B, ModernBERT, and NeoBERT. In this section, we present *latency* (seconds per forward pass) for the same encoders. As noted in Section 5.4, Avey is recent and lacks a fused-kernel (CUDA/Triton) implementation. Accordingly, we measure Avey-B's latency using both an *eager* PyTorch implementation (*Avey-B-eager*) and `torch.compile` (*Avey-B-torch-compile*). By contrast, both ModernBERT and NeoBERT have optimized implementations using FlashAttention (Dao et al., 2022). We therefore report their latencies *with* and *without* FlashAttention, and denote the resulting variants as *sys-optimized* and *sys-unoptimized*, respectively.

As with throughput, Avey-B achieves consistently lower latency and markedly superior long-context scaling (see Fig. 4 (a)), underscoring its computational efficiency even in the absence of a fused kernel. To quantify long-context behavior, we again fit a power-law model, $L(N) \propto N^{\beta}$, where N denotes the sequence length and larger exponents β indicate worse scaling. Under the optimized setting, ModernBERT-sys-optimized and NeoBERT-sys-optimized exhibit $\beta_{\text{ModernBERT}} = 1.17$ and $\beta_{\text{NeoBERT}} = 1.20$, reflecting the bandwidth and memory-pressure limitations inherent to quadratic attention. In contrast, Avey-B-torch-compile attains a substantially milder exponent of $\beta_{\text{Avey-B}} = 0.68$, and delivers more than a $3\times$ and $10\times$ latency advantage over ModernBERT-sys-optimized and NeoBERT-sys-optimized, respectively, at 96k tokens.

The unoptimized setting further accentuates these differences (see Fig. 4 (b)). ModernBERT-sys-unoptimized and NeoBERT-sys-unoptimized exhibit substantially steeper latency growth, with exponents $\beta_{\text{ModernBERT}} = 1.42$ and $\beta_{\text{NeoBERT}} = 1.63$, and both models encounter out-of-memory failures well before the maximum tested sequence length. In contrast, Avey-B-eager achieves the shallowest growth of all configurations, with $\beta_{\text{Avey-B}} = 0.58$, and maintains stable latency across the entire sequence-length range. These results confirm that Avey-B's latency advantage is structural, especially since its neural processor depends on split size rather than global sequence length, yielding linear $\mathcal{O}(N)$ scaling and robust long-context performance even in the absence of compiler- or kernel-level optimizations.

J Cross-Seed Variance Analysis

Table 11: Standard deviations across 10 random seeds for all evaluated encoders and benchmarks.

	Model	SC			TC			QA			IR		
		MNLI	QQP	SST-2	CONLL	Onto.	UNER	ReCoRD	SQuAD	SQuADv2	MLDR	MSMARCO	NQ
Base	Avey-B	0.92	0.12	0.97	0.71	0.12	2.65	0.67	0.17	0.47	0.67	1.34	0.75
	BERT	0.17	0.16	0.31	1.10	0.31	0.69	3.70	0.53	0.32	1.22	0.73	1.44
	RoBERTa	0.13	0.10	0.38	0.25	0.14	0.60	0.42	0.11	0.19	0.32	1.02	0.72
	ModernBERT	0.37	0.12	0.53	0.24	0.11	0.45	0.70	2.36	0.29	1.40	1.39	2.18
M	NeoBERT	0.40	0.14	1.20	0.24	0.17	0.47	5.98	0.91	0.66	4.70	4.30	9.48
Large	Avey-B	0.20	0.43	0.52	0.33	0.10	1.06	0.27	0.15	0.30	1.03	1.77	1.06
	BERT	0.28	8.24	0.98	0.37	0.13	0.80	2.47	0.97	0.58	0.94	1.54	1.01
	RoBERTa	0.16	0.20	0.41	0.26	0.10	0.61	0.26	0.33	0.18	0.50	1.58	0.74
	ModernBERT	0.18	0.08	0.35	0.50	0.14	3.67	17.79	0.25	1.35	2.27	1.70	3.06

To complement the median results reported in Table 2, we further evaluate each model's robustness by examining its sensitivity to random initialization. As described in Section 5.1, for every benchmark in the SC, TC, QA, and IR categories, we swept four learning rates and fine-tuned each configuration using 10 independent random seeds. While Table 2 reports the *median* performance across seeds at the *best* learning rate for each benchmark, we additionally compute the standard deviation (SD) across the 10 runs for each model–benchmark pair. These SD values quantify the variability induced by initialization and provide an additional perspective on optimization stability and robustness beyond median performance.

At the *base* scale (and *medium* for NeoBERT), RoBERTa exhibits the lowest overall variance, consistent with its well-established fine-tuning stability. Avey-B ranks second, followed by ModernBERT, BERT, and NeoBERT, in that order. Across most benchmarks, Avey-B maintains tightly concentrated variances, with the exception of UNER, where a single outlier resulted in higher variability (SD = 2.65).

At the *large* scale, the differences in stability become more pronounced. ModernBERT, despite strong median performance, exhibits substantial instability on several benchmarks (most notably ReCoRD, UNER, and NQ), suggesting high sensitivity to initialization arising from its alternating attention pattern and extended context window. Likewise, BERT demonstrates occasional catastrophic variance spikes (e.g., QQP with SD = 8.24), indicating susceptibility to poor optimization minima. In contrast, Avey-B maintains uniformly low SDs across nearly all benchmarks, with no signs of pathological instability. Its variances remain tightly bounded (typically below 1.06), often surpassing most Transformer-based baselines and again ranking just behind RoBERTa.

These variance measurements show that Avey-B is among the most statistically consistent encoders in our evaluation. We attribute this robustness to three core architectural principles: (1) the decoupling of static and dynamic layers, which prevents destructive interactions between fixed parameters and similarity scores; (2) row-normalized similarity matrices, which stabilize activation magnitudes and ensure well-behaved gradient flow; and (3) neural compression, which filters out irrelevant signals in retrieved contexts. Collectively, these mechanisms reduce sensitivity to initialization and foster smoother optimization dynamics, accounting for Avey-B's consistently low variance across tasks.

Table 12: Needle-in-a-haystack (NIAH-1) accuracy across sequence lengths from 1k to 96k for several encoders at different scales (M = Medium; OOM = Out-of-Memory).

	Model	NIAH-1							
		1k	2k	4k	8k	16k	32k	64k	96k
Base	Avey-B	79.41	79.21	78.94	79.19	78.91	77.73	77.18	75.72
Base	ModernBERT	67.74	67.64	68.31	70.67	–	–	–	–
M	NeoBERT	79.65	79.13	74.73	–	–	–	–	–
Large	Avey-B	79.69	79.24	79.03	79.58	79.44	78.44	76.76	76.06
Large	ModernBERT	68.80	67.52	67.20	OOM	–	–	–	–

Table 13: Needle-in-a-haystack (NIAH-2) accuracy across sequence lengths from 1k to 96k for several encoders at different scales (M = Medium; OOM = Out-of-Memory).

	Model	NIAH-2							
		1k	2k	4k	8k	16k	32k	64k	96k
Base	Avey-B	78.29	79.40	79.77	78.53	78.70	75.50	73.78	71.86
Base	ModernBERT	66.99	67.25	69.49	70.48	–	–	–	–
M	NeoBERT	79.61	79.52	80.07	–	–	–	–	–
Large	Avey-B	78.94	79.48	79.99	78.71	79.07	78.31	74.47	74.54
Large	ModernBERT	66.96	67.29	68.07	OOM	–	–	–	–

K Long-Range Benchmark Results

In this section, we evaluate the long-context capabilities of Avey-B, ModernBERT, and NeoBERT using a synthetic needle-in-a-haystack (NIAH) benchmark formulated as an extractive question–answering (QA) task augmented with position-sensitive reasoning. Each instance consists of a passage of a specified length (e.g., 96k tokens) filled with random distractor tokens and *one* or *more* key–value pairs, where the value constitutes the "needle." The query contains only the key, and the model must extract the corresponding value from the passage.

In the single-needle setting, the task measures a model's ability to semantically locate the correct span within an extremely long sequence. In the multi-needle setting, all key–value pairs share the same key, and the query explicitly requests the n^{th} occurrence. This removes any semantic disambiguation and introduces a position-sensitive reasoning requirement, where the model must identify all candidate spans and reason over their order to select the correct needle.

The evaluation set comprises 40% single-needle (pure long-context QA) and 60% two-needle (position-sensitive reasoning) examples, thereby jointly assessing semantic retrieval and positional reasoning under extreme sequence lengths, with the latter emphasized by design. We further construct two variants of the benchmark with different classes of randomly generated needles, namely, alphanumeric (NIAH-1) and numeric (NIAH-2), following the setup introduced in Avey (Hammoud & Acharya, 2025).

Tables 12 and 13 illustrate results for Avey-B *base* and *large*, ModernBERT *base* and *large*, and NeoBERT *medium* (the only publicly available size) on NIAH-1 and NIAH-2 across sequence lengths from 1k to 96k tokens. For ModernBERT and NeoBERT, we show results only up to their respective trained context windows (i.e., 8k and 4k tokens). In contrast, Avey-B imposes no fixed maximum sequence length and generalizes seamlessly beyond its trained 2,048-token context window, enabling evaluation up to 96k tokens.

On NIAH-1 (Table 12), Avey-B exhibits strong robustness and scalability relative to ModernBERT and NeoBERT. Both Avey-B *base* and *large* maintain near-constant accuracy from 1k to 96k tokens, with only a modest 3–4 point decrease over a $96\times$ increase in sequence length. This stability demonstrates that Avey-B effectively resolves long-range dependencies and generalizes far beyond its trained context window. By comparison, ModernBERT and NeoBERT cannot operate beyond

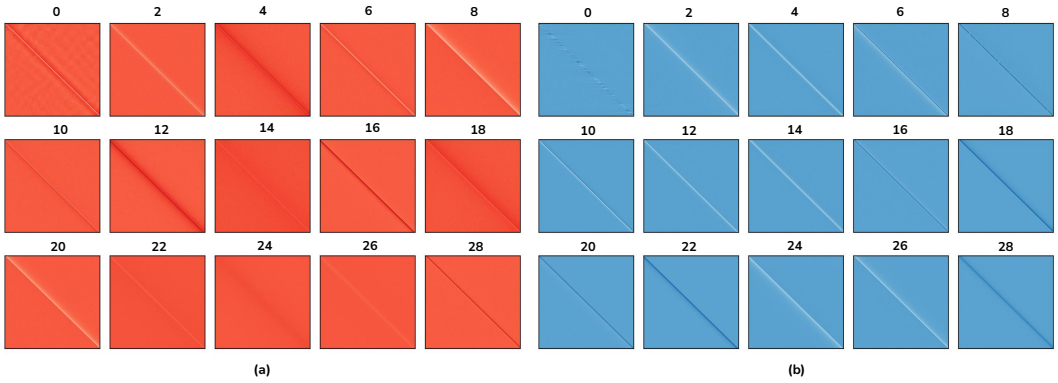

Figure 5: Learned static cross-embedding projection matrices for the (a) *coupled* configuration (left or red) with 15 matrices uniformly subsampled from 30 static layers and (b) *decoupled* configuration (right or blue) with all 15 static matrices (dynamic and static layers are interleaved, hence, only 15 static matrices exist). For comparability, we display 15 layers per panel. The coupled setting exhibits diffuse, more homogeneous patterns (e.g., see layers 14, 22, 24, and 26) suggestive of redundancy, whereas the decoupled setting shows sharper, more heterogeneous structure and variability in spread, indicating greater representational diversity.

their 8k-token and 4k-token trained windows, respectively. NeoBERT matches Avey-B at very short contexts (1–2k) but drops by roughly 5 points at 4k, while ModernBERT lags behind Avey-B by 10–12 points even at short sequence lengths[2]. Moreover, ModernBERT *large* fails at 8k tokens due to out-of-memory issues even on NVIDIA B200 GPUs using the smallest feasible batch size.

Results on NIAH-2 (Table 13) mirror the trends observed on NIAH-1 and further reinforce Avey-B's long-context robustness. Both Avey-B *base* and *large* maintain strong performance across extreme sequence lengths, with Avey-B *base* decreasing from 78.3 at 1k to 71.9 at 96k tokens, and Avey-B *large* remaining similarly stable (78.9 $\rightarrow$ 74.5). ModernBERT, by contrast, trails Avey-B by 9–12 points at short contexts and fails at 8k tokens due to memory limitations, preventing any long-context evaluation. NeoBERT remains competitive at very short lengths (1–4k) but, like ModernBERT, cannot operate beyond its 4k-token window, and therefore cannot be evaluated in the long-context regime.

In summary, Avey-B is the *only* model capable of sustaining high accuracy up to 96k tokens on this question–answering, reasoning-intensive benchmark, despite being trained with a context window of only 2,048 tokens. These results demonstrate that Avey-B not only generalizes far beyond its trained context width, but also preserves long-range reasoning fidelity in regimes where existing Transformer-based encoders either fail to extrapolate or collapse entirely.

L Coupled vs. Decoupled Layers: A Statistical Analysis

We now analyze the learned cross-embedding projection matrices (say, $\mathbf{V}$) for the *coupled* and *decoupled* Avey-B models from the ablation study in Appendix H. Table 14 reports summary statistics for each model. In the coupled case, we observe a clear *positivity bias*, especially in deeper layers, wherein the fraction of positive entries (i.e., the number of positive weights divided by the total number of weights) approaches one in several layers (in layers 8 and 13, it indeed hit 1). This bias can be explained as follows. Because the enricher employs a nonnegative activation (i.e., ReLU^2), the contextualizer's similarity matrix (say, $\mathbf{S}$) is elementwise nonnegative. As such, the coupled mixing $\mathbf{M} = \mathbf{V} \odot \mathbf{S}$ inherits its *signs* entirely from $\mathbf{V}$. Any negative entry in $\mathbf{V}$ flips a large positive similarity into a negative contribution, violating *monotonicity with respect to relevance* (see Appendix A) and degrading training. The optimizer therefore pushes $\mathbf{V}$ toward nonnegativity to avoid these destructive sign inversions, yielding the observed late-layer collapse toward positive weights.

[2]For ModernBERT versus NeoBERT, we hypothesize that the consistently lower scores of ModernBERT stem from its local–global alternating attention pattern, compared to the full bidirectional self-attention used in NeoBERT.

Despite this positivity bias, a nontrivial fraction of negative entries persists in the coupled model (see Table 14 again). This residual negativity is precisely the failure mode our hypothesis predicts, that is, wherever a neuron retains negative weights, large positive similarities can be inverted into negative contributions, yielding local violations of relevance monotonicity.

By contrast, in the decoupled case the dynamic layers alone produce the mixing weights. These weights are normalized and nonnegative by construction, so monotonicity is enforced at the similarity operator. The static layers are learned separately and no longer need to be driven into nonnegativity to preserve monotonicity. As shown in Table 14, this yields a near-zero mean with roughly balanced positive and negative weights (without the late-layer positivity bias), retains inhibitory patterns (i.e., learned negative influences) where useful, and avoids the sign-flip failure mode.

Beyond sign distribution, the two models also diverge in the *dispersion* of their weights. Coupled matrices exhibit reduced standard deviation across layers, indicating more stable transformations that converge toward smooth and homogeneous patterns. Decoupled matrices, by contrast, sustain larger fluctuations, admitting both stronger positive and stronger negative values. This higher variance may reflect greater representational flexibility. Norm statistics supports this interpretation, whereby coupled matrices accumulate larger ℓ_1 norm, distributing weight more evenly across entries, whereas decoupled matrices attain slightly higher ℓ_2 values, implying that fewer entries dominate with sharper magnitudes.

Qualitatively, the static matrices in both variants exhibit Toeplitz-like (approximately shift-invariant) structure reminiscent of gMLP (Liu et al., 2021) (see Fig. 5). As in gMLP, where such patterns emerge without an explicit prior, our static layers converge to diagonally dominant, near-diagonal matrices indicative of locality. This alignment suggests that locality-preserving, Toeplitz-like structure can arise naturally in architectures that employ fixed, input-independent transformations to stabilize and scaffold subsequent dynamic computations.

In summary, *coupling* tends to regularize the cross-embedding projections toward homogeneous, nearly nonnegative transformations, whereas *decoupling* promotes healthy diversity and sharper structure, while preserving monotonicity with respect to relevance.

Table 14: Layer statistics for coupled vs. decoupled settings. For comparability, we display 15 layers per setting. For the coupled setting, we uniformly subsampled 15 layers from 30 static layers. For the decoupled setting, *all* the 15 static layers are shown (dynamic and static layers are interleaved, hence, only 15 static layers exist). The coupled setting exhibits *positivity bias* (see the "fraction of positive" column), while the decoupled setting demonstrates more *balanced* positive and negative weights, indicating greater representational diversity.

Coupled

Layer	Mean	Std	Min	Median	Max	Abs. Mean	L1 Norm	L2 Norm	Frac. Pos.	Frac. Neg.
1	0.00	0.12	−1.67	0.00	1.20	0.05	3369.19	30.68	0.47	0.53
2	−0.01	0.11	−1.55	0.00	0.30	0.04	2345.75	27.73	0.53	0.47
3	0.08	0.09	−0.23	0.06	0.68	0.09	5906.35	31.56	0.90	0.10
4	0.00	0.10	−1.19	0.01	0.29	0.03	2211.32	24.42	0.61	0.39
5	−0.03	0.13	−1.09	0.00	0.15	0.06	3724.35	33.82	0.55	0.45
6	0.01	0.08	−1.47	0.00	0.63	0.03	1963.87	21.33	0.57	0.43
7	0.03	0.11	−0.29	0.00	1.00	0.06	3959.52	30.11	0.52	0.49
8	0.11	0.04	−0.14	0.11	0.33	0.11	7525.47	31.17	1.00	0.00
9	0.00	0.10	−0.38	−0.01	1.43	0.04	2300.72	25.97	0.34	0.66
10	0.09	0.06	−0.07	0.08	0.38	0.09	5844.50	27.45	0.98	0.02
11	−0.02	0.10	−0.90	0.01	0.12	0.04	2604.39	26.53	0.59	0.41
12	0.07	0.02	−0.04	0.07	0.16	0.07	4697.84	19.12	0.98	0.02
13	0.05	0.03	−0.04	0.05	0.21	0.05	3487.26	15.28	1.00	0.00
14	0.03	0.02	−0.14	0.03	0.18	0.04	2293.24	9.56	0.95	0.05
15	0.00	0.07	−0.39	−0.01	0.83	0.03	1912.78	18.29	0.34	0.66
Avg.	0.03	0.08	−0.64	0.03	0.53	0.06	3609.77	24.87	0.69	0.31

Decoupled

Layer	Mean	Std	Min	Median	Max	Abs. Mean	L1 Norm	L2 Norm	Frac. Pos.	Frac. Neg.
1	0.00	0.08	−0.98	0.00	1.04	0.04	2327.62	21.31	0.51	0.49
2	−0.02	0.12	−1.27	0.00	0.23	0.05	3065.94	30.83	0.51	0.49
3	−0.01	0.12	−1.93	0.01	0.27	0.04	2312.23	30.24	0.66	0.34
4	−0.01	0.12	−1.01	0.01	1.35	0.04	2825.07	29.60	0.60	0.40
5	0.00	0.10	−0.50	−0.01	1.70	0.03	2129.54	26.59	0.42	0.58
6	0.00	0.11	−2.09	0.00	0.68	0.03	1978.08	28.17	0.61	0.39
7	0.00	0.11	−1.60	0.01	0.33	0.03	2050.08	27.01	0.69	0.31
8	−0.01	0.11	−1.22	0.01	0.30	0.03	2104.69	27.52	0.70	0.30
9	0.00	0.09	−0.26	0.00	1.37	0.03	1697.87	23.67	0.42	0.58
10	0.01	0.12	−0.34	−0.01	1.27	0.03	2145.28	30.16	0.34	0.66
11	0.00	0.09	−0.28	−0.01	1.18	0.03	1775.56	23.28	0.35	0.65
12	0.01	0.11	−0.22	−0.01	1.62	0.03	2019.32	29.24	0.33	0.67
13	−0.02	0.11	−1.35	0.00	0.24	0.04	2637.36	28.99	0.58	0.42
14	−0.02	0.10	−1.04	0.00	0.18	0.04	2292.65	26.27	0.61	0.39
15	0.01	0.08	−0.06	0.00	0.82	0.03	1779.38	19.60	0.51	0.49
Avg.	0.00	0.10	−0.94	0.00	0.84	0.03	2209.38	26.83	0.52	0.48